

RESEARCH ARTICLE

10.1002/2015JE004908

Key Points:

- Reexamine proposed interior configurations for Mercury
- Constrain the solid core volume by the amount of observed planetary contraction
- Constrain the feasible range for the composition of Mercury's core

Correspondence to:

J. S. Knibbe,
j.s.knibbe@vu.nl

Citation:

Knibbe, J. S., and W. van Westrenen (2015), The interior configuration of planet Mercury constrained by moment of inertia and planetary contraction, *J. Geophys. Res. Planets*, 120, 1904–1923, doi:10.1002/2015JE004908.

Received 28 JUL 2015

Accepted 26 OCT 2015

Accepted article online 28 OCT 2015

Published online 25 NOV 2015

The interior configuration of planet Mercury constrained by moment of inertia and planetary contraction

J. S. Knibbe¹ and W. van Westrenen¹
¹Faculty of Earth and Life Sciences, VU University Amsterdam, Amsterdam, Netherlands

Abstract This paper presents an analysis of present-day interior configuration models for Mercury considering cores of Fe-S or Fe-Si alloy, the latter possibly covered by a solid FeS layer, in light of the improved limit of planetary contraction of 7 km derived from Mercury Surface, Space ENvironment, GEochemistry, and Ranging observations of surface landforms. Density profiles, generated by a Monte Carlo approach, are constrained by Mercury's mass, polar moment of inertia (C), fraction of polar moment corresponding to its outer solid shell (C_m/C), and observed planetary contraction. Results show that the outer liquid core boundary is constrained to 1985–2090 km in radius, where large radii correspond to high Si and S core contents and high mantle densities or the presence of an FeS layer at the top of the outer core. The bulk core S and Si contents are within 2.8–8.9 wt % and above 8.5 wt %, respectively, where an increase of light element core content correlates positively with mantle density and core size. The size of the inner core is constrained by the observed planetary contraction to below 1454 or 1543 km in radius for bulk cores rich in S (near 8.9 wt %) or Si (near 25 wt %), respectively. For cores poor in light elements, inner cores up to 1690 km in radius remain consistent with the observed planetary contraction. Finally, we show that solid FeS at outer core conditions, previously argued to float on liquid Fe-S, may be denser than the residual liquid. This implies that a separate mechanism may be required to maintain an FeS layer at the suggested location.

1. Introduction

Prior to the Mariner 10 (Mercury flybys in 1974 and 1975) and Mercury Surface, Space ENvironment, GEochemistry, and Ranging (MESSENGER) (Mercury flybys in 2008–2009 and in orbit from 2011 to 2015) space missions, our knowledge of the innermost planet was limited to its size, basic orbital dynamics, and the anomalously high bulk density of 5427 kg m^{-3} [Ash *et al.*, 1971; Anderson *et al.*, 1987] indicative of a large iron (Fe)-rich core.

The discovery of a magnetic field intrinsic to Mercury [Ness *et al.*, 1974, 1975] and visual confirmation of the prior radar observation by Pettengill and Dyce [1965] that Mercury is locked in a 3:2 spin-orbit resonance state are among the major accomplishments of the Mariner 10 mission [Klaasen, 1975]. Mercury's magnetic field was a strong but nonconclusive indication that Mercury's core is partially liquid [e.g., Stevenson *et al.*, 1983]. Later, the amplitude of forced librations in longitude direction of Mercury's surface was determined using radar speckle measurements [Margot *et al.*, 2007]. Because the solar gravitational torque is too small to force librations of the observed amplitude for the whole of Mercury, an outer solid shell must be decoupled from its interior. This confirms the presence of a global liquid internal layer [Margot *et al.*, 2007], which has important implications for the current interior temperature, structure, and composition of the planet. In particular, it was suggested that the core may include light elements sulfur (S) or silicon (Si), which lower the melting temperature with respect to a pure Fe core and may have prevented the core from total solidification [e.g., Stevenson, 1983; Malavergne *et al.*, 2010].

An additional radar observation is the near-constant tilt of Mercury that is approximately coplanar with the orbit normal and the ecliptic normal. Combined with the locked spin-orbit resonance, this indicates that Mercury is in or very near a Cassini state 1. Consequently, the number of coupled variational equations that describes the planet's rotational dynamics is reduced from six to four [Peale, 1973, 1988]. Assuming that the core does not follow the 88th day libration period of the outer solid shell but does follow the perihelion precession with a period of $\sim 250,000$ years, a formulation for the planet's polar moment of inertia (C) and the fraction of the polar moment of inertia that corresponds to the outer librating solid shell (C_m/C) has been deduced in terms of the planet's obliquity, the amplitude of forced librations in longitude, and the

gravitational harmonics C_{22} and C_{20} [e.g., Peale, 1976, 1988; Peale *et al.*, 2002]. Recent determination of C_{22} and C_{20} , obtained by radio tracking of the MESSENGER spacecraft [Smith *et al.*, 2012; Mazarico *et al.*, 2014], and improved estimates for the obliquity and the amplitude of forced librations of the outer solid shell [Margot *et al.*, 2012] have yielded the normalized polar moment of inertia (C/MR^2) and C_m/C of 0.349 ± 0.014 and 0.424 ± 0.024 , respectively [Mazarico *et al.*, 2014]. These parameters constrain the density distribution of Mercury's interior and the size of the outer solid shell in particular. Van Hoolst *et al.* [2012] and Dumberry *et al.* [2013] showed that the 88 day librations of the core are significant if the inner core is large. In that case, the value of C_m/C as given by Margot *et al.* [2012] and Mazarico *et al.* [2014] would be overestimated by up to 5%.

Among the many accomplishments of the MESSENGER mission are compositional measurements of major element abundances on Mercury's surface [e.g., Nittler *et al.*, 2011; Weider *et al.*, 2012, 2014] and global high-resolution imaging of the planet's surface [e.g., Byrne *et al.*, 2014]. Low measured surface abundances of Fe combined with Mercury's large Fe-rich core are indicative of a low oxygen fugacity (3–6.5 log units below the iron-wustite buffer) for the planet's bulk composition [e.g., Malavergne *et al.*, 2010; McCubbin *et al.*, 2012; Zolotov *et al.*, 2013]. Other compositional features include an unusual high S content of the surface. High-pressure experiments have shown that concentrations of S and Si in core-forming metal alloys in equilibrium with the silicate mantle are substantial for such oxygen-poor compositions [e.g., Siebert *et al.*, 2004; Malavergne *et al.*, 2010; Chabot *et al.*, 2014]. These are strong indications in favor for the hypothesis that one or both of these light elements are present in Mercury's core.

Prior to MESSENGER's global high-resolution imaging, estimates of the planet's radial planetary contraction by identification and examination of contraction features (fault and fold structures) ranged up to 3 km [e.g., Strom *et al.*, 1975; Watters *et al.*, 1998, 2009; Di Achille *et al.*, 2012]. These observational estimates were in substantial disagreement with the larger amount of contraction of ~4 km to ~10 km that the planet should have endured due to long-term planetary cooling according to a wide range of thermal evolution models [e.g., Solomon, 1977; Schubert *et al.*, 1988; Van Hoolst and Jacobs, 2003; Dombard and Hauck, 2008; Grott *et al.*, 2011; Tosi *et al.*, 2013]. Recently, this discrepancy has come closer to being resolved by a thorough examination of MESSENGER's high-resolution images with global coverage that yields global contraction estimates up to 7 km in radius [Byrne *et al.*, 2014].

Many have studied the thermomechanical evolution of the planet [e.g., Solomon, 1977; Schubert *et al.*, 1979; Stevenson *et al.*, 1983; Schubert *et al.*, 1988; Spohn, 1991; Breuer *et al.*, 2007; Grott *et al.*, 2011; Michel *et al.*, 2013; Tosi *et al.*, 2013] or the present-day interior configuration [e.g., Jeffreys, 1936; Macdonald, 1962; Plagemann, 1965; Lyttleton, 1969; De Jager, 1971; Harder and Schubert, 2001; Hauck *et al.*, 2007; Riner *et al.*, 2008; Rivoldini *et al.*, 2009; Dumberry, 2011; Hauck *et al.*, 2013; Rivoldini and Van Hoolst, 2013; Padovan *et al.*, 2014; Dumberry and Rivoldini, 2014]. The first type of studies relates planetary evolution scenarios covering the time span of our solar system to the evolution of interior temperatures, structure, and core solidification. They yield, for example, estimates of planetary contraction induced by planetary cooling and core solidification. Most of these earlier studies model the contraction that results from solidification of a pure Fe core [e.g., Solomon, 1977; Schubert *et al.*, 1988; Hauck *et al.*, 2004], whereas most more recent studies incorporated the effect of S on planetary contraction induced by core solidification [Van Hoolst and Jacobs, 2003; Grott *et al.*, 2011]. Tosi *et al.* [2013] did not examine the contribution of core solidification to planetary contraction but focused on total volume changes associated with thermal expansion/contraction, partial melting, and differentiation of a cooling Mercury. The effect of Si as a core constituent on planetary contraction has not been studied, although the presence of silicon (Si) in the core has been suggested repeatedly in the past few years [Malavergne *et al.*, 2010; Hauck *et al.*, 2013].

C/MR^2 and C_m/C have constrained the location of the outer liquid boundary (OLB), equivalent to the base of the librating outer solid shell, to around 2020 ± 50 km in radius [Hauck *et al.*, 2013; Rivoldini and Van Hoolst, 2013]. Smith *et al.* [2012] and Hauck *et al.* [2013] suggested that a solid FeS layer may reside on top of the liquid portion of the core and take part in the outer solid shell. Consequently, the core-mantle boundary (CMB) would be located at a larger radius. Whether the CMB is identical or similar to the well-constrained OLB (and the size of the crust + mantle is approximately known) thus depends on the existence and thickness of an FeS layer. The location of the inner core boundary (ICB) is poorly constrained by C/MR^2 and C_m/C , especially if the density difference between solid and liquid core material is small

or the inner core is not particularly large. *Dumberry* [2011], *Van Hoolst et al.* [2012], and *Dumberry et al.* [2013] examined how different inner core sizes would induce “free” libration modes of different periods in decadal timescales. Generally, they conclude that a large inner core increases the period of this free libration from ~11 years for an inner core of <1000 km in radius to ~17 years for an inner core of 1900 km in radius. Long-term series of libration observations may, thus, eventually yield constraints on the size of an inner core. Future spacecraft observations with high measurement precision will be particularly useful to detect such libration modes. Libration modes of similar long-term frequencies induced by gravitational interactions with Jupiter may, however, complicate the interpretations of such observations [*Yseboodt et al.*, 2013, and references therein].

In the absence of observational constraints on the size of Mercury’s inner core today, various modeling studies aim to constrain the inner core size and the core’s chemical composition by relating feasible temperature profiles to experimentally determined iron-sulfur melting behavior [*Dumberry and Rivoldini*, 2014] or by relating the size of the inner core to equivalent planetary contraction that results from core solidification and planetary cooling [e.g., *Rivoldini et al.*, 2014]. *Dumberry and Rivoldini* [2014] have, for example, recently constrained the size of the inner core to a maximum radius of 1325 ± 250 km by simultaneously considering feasible temperature profiles and interior configurations consistent with C/MR^2 and C_m/C for cores of binary Fe-S alloys, taking into account the presence of Fe-snow zones that likely occur in Mercury’s liquid core in case it is S rich. To date no study has been performed to constrain the interior configuration simultaneously by the corresponding amount of planetary contraction, C/MR^2 and C_m/C .

In this study we reexamine implications for the interior structure of Mercury of three proposed end-member interior configurations by generating a large number of density profiles consistent with the planet’s bulk density in a Monte Carlo approach similar to *Harder and Schubert* [2001] and *Hauck et al.* [2007, 2013]. For each density profile, the corresponding C/MR^2 and C_m/C and the amount of radial contraction that directly results from core solidification (ΔR_{cs}) are calculated. The known C/MR^2 and C_m/C and the observed radial planetary contraction for Mercury constrain the generated profile set, in particular the boundary locations and the composition of the core. We do not estimate the total volume changes that are associated with thermal expansion/contraction, partial melting, and differentiation of a cooling Mercury but discuss implications of these volume changes by taking into consideration the results of *Grott et al.* [2011] and *Tosi et al.* [2013]. As detailed in the following section, the interior configurations considered here include binary Fe-S or Fe-Si cores and Fe-Si core with a solid FeS layer positioned between the silicate mantle and the outer core.

2. Method

2.1. The Interior Configuration Models

The three main interior configuration models examined in this paper assume a silicate mantle and crust and a partially liquid core of Fe-S or Fe-Si composition, the latter possibly overlain by a layer of solid FeS (similar to the models described by *Hauck et al.* [2013]). Only binary core alloys are considered, because the density of ternary metal systems at high pressures and high temperatures is insufficiently known at present. Additionally, the segregation of ternary melts toward two pseudo-binary liquid layers is likely for the core compositions considered here [e.g., *Sanloup and Fei*, 2004; *Siebert et al.*, 2004; *Morard et al.*, 2008; *Morard and Katsura*, 2010; *Hillgren and Fei*, 2013].

2.1.1. Fe-S Model

S has been often suggested to alloy with Fe in Mercury’s core because its decreasing effect on liquidus temperatures may explain the presence of liquid material in Mercury’s interior today. Additionally, the S abundance of Mercury’s surface appears to be higher than that of the surface of any other terrestrial planet [e.g., *Nittler et al.*, 2011; *Weider et al.*, 2012]. The Fe-S model assumes a core of binary Fe-S composition with bulk core S contents below that of the eutectic composition, which is determined at around 15 wt % S for this pressure range [e.g., *Fei et al.*, 2000; *Chudinovskikh and Boehler*, 2007], with core solidification starting at the planet’s center. Because the fractionation of S into solid is negligible for S contents below 15 wt % at pressures relevant for Mercury’s interior [e.g., *Li et al.*, 2001], the residual liquid enriches in S during core solidification. In case the ICB attains pressures higher than 18 GPa and the residual liquid attains the eutectic composition, Fe₃S will precipitate and form an outer layer on the inner core [*Fei et al.*, 2000]. Because Fe₃S has a higher density than liquid of similar composition, it has a larger contribution to Mercury’s

Table 1. The Free-Parameter Space for the Interior Configuration Models^a

Parameter/Model	Fe-Si	Fe-S	Fe-Si-FeS
T_{OLB} (K)	1600–2000	1600–2000	1600–2000
R_{CMB} (km)	1700–2250	1700–2250	1750–2300
R_{OLB} (km)	R_{CMB}	R_{CMB}	$R_{\text{CMB}} - (R_{\text{CMB}} - 200)$
R_{ic} (km)	$0 - R_{\text{CMB}}$	$0 - R_{\text{CMB}}$	$0 - R_{\text{OLB}}$
R_{Fe3S} (km)	-	$0 - R_{\text{ic}}$	-
X_{S} (fraction)	-	0–0.15	-
X_{Si} (fraction)	0–0.25	-	0–0.25
$\rho_{0, \text{mantle}}$ (kg m^{-3})	2800–3600	2800–3600	2800–3600

^a T_{OLB} is the temperature at the OLB, which equals the CMB for the Fe-S and Fe-Si models. R_{OLB} denotes the outer liquid boundary, R_{ic} the inner liquid boundary, and R_{Fe3S} denotes the Fe_3S -Fe boundary within the solid inner core. X_{S} and X_{Si} denote the S and Si contents in the total core in terms of weight fraction, respectively. $\rho_{0, \text{mantle}}$ denotes the reference density used in the EOS to parametrize mantle density (equation (1)).

moment of inertia compared to that of a liquid with similar S content. For this reason, a configuration with high S content may potentially be consistent with Mercury's moment of inertia if it contains an Fe_3S layer, whereas results of Rivoldini and Van Hoolst [2013] indicate that the bulk core S content is bounded from above at 6.3 wt % based on models without an Fe_3S layer. By solidification at the eutectic, the composition of the residual liquid will not change significantly. For this reason, the Fe-S model assumes a solid inner core of one or two solid layers, pure Fe at the center and possibly Fe_3S as the outer solid shell, and a liquid outer core of Fe-S alloy. If the Fe_3S layer is modeled, we force the liquid outer core to contain 15 wt % of S. The CMB is assumed to be located between 1700 km and 2200 km in radius, and the ICB is between the CMB and the planet's center. In case an Fe_3S layer is modeled, a solid Fe- Fe_3S boundary will be located between the center of the planet and the ICB.

2.1.2. Fe-Si Model

Si is the most abundant element on Mercury's surface and likely among the most abundant elements in its mantle. Several experimental studies have indicated that the fractionation of Si into metal during metal-silicate equilibration increases significantly in the low-oxygen environments that are proposed for Mercury [e.g., McCoy et al., 1999; Berthet et al., 2009; Malavergne et al., 2010]. The Fe-Si model assumes that Si is the only element to significantly alloy with iron in the core during core-mantle segregation. In this case it is likely that core solidification will initiate at the center of the planet, where it attains maximal pressure. Experimental studies show that solid-liquid fractionation in the binary Fe-Si system at high pressure occurs nonpreferentially in terms of elemental abundances [e.g., Kuwayama and Hirose, 2004]. For this reason, we define the composition of solid core equal to that of the liquid (and bulk) core. Similar to the Fe-S model, the CMB is assumed between 1700 km and 2200 km in radius and the ICB is assumed between the CMB and the planet's center. The compositional range for the core in this model is between pure Fe and 25 wt % Si.

2.1.3. Fe-Si-FeS Model

In case both S and Si alloy with Fe during core-mantle segregation, the immiscibility in Fe-S-Si liquids [e.g., Sanloup and Fei, 2004; Siebert et al., 2004; Morard et al., 2008; Morard and Katsura, 2010; Hillgren and Fei, 2013] likely causes these liquids to segregate in upper S-rich Fe-S-Si and lower Si-rich Fe-S-Si liquid as a result of their density contrast [e.g., Malavergne et al., 2010]. Smith et al. [2012] and Hauck et al. [2013] argued that this may result in an outer core layer sufficiently enriched in S to form solid FeS. They proposed that this FeS layer accretes to the outer solid shell. An FeSi solid inner core may solidify at the planet's center, as in the Fe-Si model. This Fe-Si-FeS model assumes an interior configuration with a solid FeSi inner core and a liquid Fe-Si outer core with Si contents below 25 wt %, covered by a solid FeS layer of maximum 200 km thickness. The CMB is assumed between 1750 km and 2300 km in radius, and the ICB is assumed between the base of the FeS layer and the planet's center.

The ranges for boundary locations corresponding to the above models, the considered ranges for mantle reference density ($\rho_{0, \text{mantle}}$), and that for CMB temperature (T_{CMB}) are listed in Table 1. The T_{CMB} range, 1600–2000 K, includes the range of feasible present-day temperatures according to thermal evolution model results of Tosi et al. [2013] and Grott et al. [2011] and is similar to results of simulations performed in Michel et al. [2013]. The implementation of these parameters is explained in sections 2.2 and 2.3.

2.2. EOS Parameters

We use the third-order Birch-Murnaghan equations of state (EOS) [e.g., *Poirier*, 2000] to characterize the density of the solid and liquid phases described in the previous section:

$$P = \frac{3K}{2} \left(\left(\frac{\rho}{\rho_0} \right)^{\frac{7}{3}} - \left(\frac{\rho}{\rho_0} \right)^{\frac{5}{3}} \right) \cdot \left(1 + \frac{3}{4} (K_d - 4) \cdot \left(\left(\frac{\rho}{\rho_0} \right)^{\frac{2}{3}} - 1 \right) \right) + \alpha K (T - T_0). \quad (1)$$

In equation (1), P is pressure, ρ is the local density, K is the material's bulk modulus, α is the material's thermal expansion coefficient, and K_d is the pressure derivative of the bulk modulus. ρ_0 is the material's reference density, and T_0 is the reference temperature of the applied EOS. In this section we motivate the EOS parameters that are applied throughout this study, as compiled in Table 2.

At pressures and temperatures relevant for Mercury's core, solid Fe exists mainly in the fcc phase [*Komabayashi and Fei*, 2010]. EOS parameters for this well-studied high-pressure phase [e.g., *Boehler et al.*, 1990; *Komabayashi et al.*, 2009] are taken from *Komabayashi and Fei* [2010]. For solid FeSi alloys we interpolate and extrapolate the EOS parameters linearly based on those of pure Fe and those of $\text{Fe}_{71}\text{Si}_{29}$ (~17 wt % Si), the latter based on high-pressure experiments ranging up to 55 GPa [*Lin et al.*, 2003]. For Si contents of around 8 wt % a phase transition in solid Fe-Si alloy has been detected between 16 GPa and 36 GPa [*Lin et al.*, 2003] but the density difference between these phases is small and considered negligible here. EOS parameters of solid Fe_3S are based on high-pressure experiments at around 21 GPa [*Fei et al.*, 2000] that have later been extended to pressures up to ~80 GPa [*Seagle et al.*, 2006]. Solid FeS is modeled only as a layer located at the top of the outer core, where pressures below ~8 GPa are attained. At these pressures and the relevant high temperatures, FeS has the NiAs-type structure (FeS V). The density of this phase was studied in *Fei et al.* [1995] and *Urakawa et al.* [2004]. Results of *Urakawa et al.* [2004] indicate that the density of this phase cannot be properly parametrized across its entire pressure range by a single EOS. Instead, they present EOS parameters for the pressure range above 11 GPa, where FeS V is referred to as FeS V (HPP), and the offset for the density of FeS V in the lower pressure range, which is referred to as FeS V (LPP), is plotted at a temperature of 1200 K [*Urakawa et al.*, 2004, Figure 3]. These results indicate that the offset between the HPP and LPP phases is large at ambient pressures and disappears at ~11 GPa. According to *Selivanov et al.* [2003], the density of FeS V at 1000 K and ambient pressure equals ~4560 kg m⁻³, which corresponds to an offset of 6.8% with respect to the EOS for FeS V (HPP). Since outer core pressures in Mercury are likely in the range of 3–7 GPa and this offset decreases with pressure, the offset is likely smaller than 6% in the relevant pressure range at 1000 K (that is, the reference temperature of the EOS). Given that the temperature at the top of the outer core in Mercury is likely higher than 1000 K at present [e.g., *Tosi et al.*, 2013; *Michel et al.*, 2013], and given that the thermal expansion coefficient of FeS V (LPP) is about twice that of FeS V (HPP) [*Urakawa et al.*, 2004], the 6% offset is likely a maximum at the conditions relevant to an FeS layer in Mercury. To account for the rather large uncertainty in the density of FeS V (LPP), we vary the reference density for FeS between 4580 kg m⁻³ and 4775 kg m⁻³, which corresponds to densities 6% and 2% below the EOS of FeS V (HPP) given in *Urakawa et al.* [2004].

For the density of pure Fe liquid we use the experimental EOS parameters presented by *Anderson and Ahrens* [1994] with the adiabatic bulk modulus translated to an isothermal bulk modulus using the Grüneisen parameter [*Balog et al.*, 2003]. Although this EOS has later been updated by integrating additional experimental results [*Komabayashi and Fei*, 2010], the latter EOS does not differ significantly for pressures relevant for Mercury's core. The EOS of *Anderson and Ahrens* [1994] has the advantage of being centered at similar reference temperatures to the other liquid EOSs used in this study. For Fe-S liquids we use an EOS from values of *Sanloup et al.* [2000] determined from X-ray absorption measurements on Fe-rich liquid with 10 wt % S, 20 wt % S, and 27 wt % S. Although that study presents experimental results for pressures only up to 6.2 GPa, sound velocity measurements up to 8 GPa [*Jing et al.*, 2014] were consistent with these values and the EOS parameters of liquid Fe-S containing 10 wt % S have been validated up to ~20 GPa by sink/float experiments [*Balog et al.*, 2003]. Given that liquid iron alloys in our study all contain 15 wt % S or less, the implementation of this EOS is suitable for most of Mercury's core. The reference density of liquid Fe-S alloys is quadratically interpolated through values of *Jing et al.* [2014], which are based on *Kaiura and Toguri* [1979], *Hixson et al.* [1990], and *Sanloup et al.* [2000]. The nonlinear relation in reference densities according to *Sanloup et al.* [2000] and *Jing et al.* [2014] seems to be based on the small S

Table 2. EOS Parameters Used in This Study^a

Parameters	Value	Unit	Source
K_{mantle}	120	GPa	Harder and Schubert [2001]
K_{dmantle}	4.25	-	Harder and Schubert [2001]
ρ_0 , mantle	2800–3600	kg m^{-3}	Hauck et al. [2013]
T_0 , mantle	440	K	Harder and Schubert [2001]
α_{mantle}	$3 \cdot 10^{-5}$	K^{-1}	Harder and Schubert [2001]
$K_{\text{Fe, solid}}$	165	GPa	Komabayashi and Fei [2010]
$K_{\text{dFe, solid}}$	5.5	-	Komabayashi and Fei [2010]
ρ_0 , Fe, solid	8170	kg m^{-3}	Komabayashi and Fei [2010]
T_0 , Fe, solid	293	K	Komabayashi and Fei [2010]
$\alpha_{\text{Fe, solid}}$	$6.4 \cdot 10^{-5}$	K^{-1}	Komabayashi and Fei [2010]
$K_{\text{Fe-Si (17 wt\%), solid}}$	141	GPa	Lin et al. [2003]
$K_{\text{dFe-Si (17 wt\%), solid}}$	5.70	-	Lin et al. [2003]
ρ_0 , Fe-Si (17 wt%), solid	7147	kg m^{-3}	Lin et al. [2003]
T_0 , FeS (V), solid	300	K	Lin et al. [2003]
$\alpha_{\text{FeS (V), solid}}$	$6.4 \cdot 10^{-5}$	K^{-1}	Lin et al. [2003]
$K_{\text{Fe3S, solid}}$	150	GPa	Fei et al. [2000]
$K_{\text{dFe3S, solid}}$	4	-	Fei et al. [2000]
ρ_0 , Fe3S, solid	7033	kg m^{-3}	Fei et al. [2000]
T_0 , Fe3S, solid	293	K	Fei et al. [2000]
$\alpha_{\text{Fe3S, solid}}$	$6.4 \cdot 10^{-5}$	K^{-1}	Fei et al. [2000]
$K_{\text{FeS (V), solid}}$	54.3	GPa	Urakawa et al. [2004]
$K_{\text{dFeS (V), solid}}$	4	-	Urakawa et al. [2004]
ρ_0 , FeS (V), solid	4872	kg m^{-3}	Urakawa et al. [2004]
T_0 , FeS (V), solid	1000	K	Urakawa et al. [2004]
$\alpha_{\text{FeS (V), solid}}$	$10.4 \cdot 10^{-5}$	K^{-1}	Urakawa et al. [2004]
$K_{\text{Fe, liquid}}$	87	GPa	Anderson and Ahrens [1994] and Balog et al. [2003]
$K_{\text{dFe, liquid}}$	5	-	Anderson and Ahrens [1994] and Balog et al. [2003]
ρ_0 , Fe, liquid	7019	kg m^{-3}	Anderson and Ahrens [1994] and Balog et al. [2003]
T_0 , Fe, liquid	1770	K	Anderson and Ahrens [1994] and Balog et al. [2003]
$\alpha_{\text{Fe, liquid}}$	$9.2 \cdot 10^{-5}$	K^{-1}	Anderson and Ahrens [1994] and Balog et al. [2003]
$K_{\text{Fe-Si (17 wt\%), liquid}}$	73	GPa	Yu and Secco [2008] and Sanloup et al. [2004]
$K_{\text{dFe-Si (17 wt\%), liquid}}$	4	-	Yu and Secco [2008] and Sanloup et al. [2004]
ρ_0 , Fe-Si (17 wt%), liquid	6000	kg m^{-3}	Yu and Secco [2008] and Sanloup et al. [2004]
T_0 , Fe-Si (17 wt%), liquid	1723	K	Yu and Secco [2008] and Sanloup et al. [2004]
$\alpha_{\text{Fe-Si (17 wt\%), liquid}}$	$9.2 \cdot 10^{-5}$	K^{-1}	Yu and Secco [2008] and Sanloup et al. [2004]
K_a , Fe-S, liquid	780.8	$\text{GPa } \chi_S^{-2}$	Sanloup et al. [2000] and Jing et al. [2014]
K_b , Fe-S, liquid	-462.4	$\text{GPa } \chi_S^{-1}$	Sanloup et al. [2000] and Jing et al. [2014]
K_c , Fe-S, liquid	85.9	GPa	Sanloup et al. [2000] and Jing et al. [2014]
$K_{\text{dFe-S, liquid}}$	5.1	-	Sanloup et al. [2000]
$\rho_{0,a}$, Fe-S, liquid	31524	$\text{kg m}^{-3} \chi_S^{-2}$	Sanloup et al. [2000] and Jing et al. [2014]
$\rho_{0,b}$, Fe-S, liquid	-20012	$\text{kg m}^{-3} \chi_S^{-1}$	Sanloup et al. [2000] and Jing et al. [2014]
$\rho_{0,c}$, Fe-S, liquid	7019	kg m^{-3}	Sanloup et al. [2000] and Jing et al. [2014]
T_0 , Fe-S, liquid	1770	K	Sanloup et al. [2000]
$\alpha_{\text{Fe-S, liquid}}$	$9.2 \cdot 10^{-5}$	K^{-1}	Sanloup et al. [2000]

^aThe reference density and bulk modulus of liquid Fe-S are parametrized as $x = x_a \cdot \chi_S^2 + x_b \cdot \chi_S + x_c$, with x the corresponding parameter and χ_S the sulfur weight fraction. Parameters of liquid Fe-Si are linearly interpolated and extrapolated using pure Fe EOS parameters [Anderson and Ahrens, 1994] and the EOS parameters for Fe-17 wt % Si [Lin et al., 2003]. The density of solid FeS is lowered by a factor between 2% and 6% with respect to the EOS parameters from Urakawa et al. [2004] listed in this table.

dependence on the ambient pressure density of liquid FeS [Kaiura and Toguri, 1979] that seems insufficient to meet the high ambient pressure density of pure Fe by linear extrapolation. Ambient pressure density measurements of Fe-rich liquids with intermediate S contents (0–36 wt % S) are lacking to conclusively validate this quadratic relation, but nonetheless, the quadratic relation seems a reasonable assumption at present. The EOS of Fe-Si liquids (up to 25 wt % Si) used here is based on the results of sink/float experiments up to 12 GPa [Yu and Secco, 2008], which differ only slightly from the results obtained by X-ray absorption measurements up to 5 GPa [Sanloup et al., 2004]. The bulk modulus of liquid Fe-S alloys is quadratically interpolated through measurements of Sanloup et al. [2000], and all other EOS parameters are linearly interpolated (Table 2).

2.3. Generation of Density Profiles

Assuming a spherically symmetric distribution of matter throughout Mercury's interior, we generate sets of internally consistent one-dimensional gravity, pressure, and density profiles with a method similar to *Harder* [1998], *Harder and Schubert* [2001], and *Hauck et al.* [2007, 2013]. For each set of profiles we fix the mantle reference density, the locations of phase boundaries, and the bulk core composition to a random value within the ranges that are considered by the four interior configuration models (Table 1). We generate the profiles by consecutively calculating mass, gravity, pressure, temperature, and density from the planet's surface toward the planet's center in steps of 1 km by iteratively solving equations (2)–(4) and (1):

$$M(r) = M(R) - 4\pi \int_r^R \rho(x) x^2 dx, \quad (2)$$

$$g(r) = \frac{G}{r^2} M(r), \quad (3)$$

$$P(r) = \int_r^R g(x) \rho(x) dx, \quad (4)$$

with M the planetary mass interior to radius r , R the planet's radius (set to 2440 km), g the local gravitational force, and G the universal gravitational constant. The initial boundary condition is the total mass of the planet $M(R)$, set to $3.3023 \cdot 10^{23}$ kg. The third-order Birch-Murnaghan EOS (equation (1)) is numerically solved for ρ by the Levenberg-Marquardt algorithm [Levenberg, 1944; Marquardt, 1963]. Equation (1) requires a temperature profile T to be defined for the mantle and core. For the mantle, *Harder and Schubert* [2001] have modeled the temperature profile in the outer solid shell of Mercury as a stepwise linear function through a lithosphere and mantle, with a temperature jump of between 0 and 300 K at the CMB to account for a thermal boundary layer. Later, *Hauck et al.* [2007], *Hauck et al.* [2013], and *Rivoldini and Van Hoolst* [2013], among others, have noted that small variations in the mantle density are of negligible influence on the moment of inertia constraints and that only the average mantle density and mantle size are of significant importance in the case of Mercury. Nevertheless, in this paper we do account for a slope in the density of the outer solid shell due to pressure and temperature effects by integrating an EOS for the mantle similar to *Harder and Schubert* [2001] with a first-order temperature profile that we take linear in the outer solid shell given a surface temperature of 440 K and a temperature jump of 150 K at the CMB, or the OLB for the Fe-Si-FeS model, to CMB (or OLB) temperatures given in Table 1. A temperature profile in the liquid core is often approximated by an adiabatic temperature profile. As long as the adiabatic gradient is smaller than the melting curve of the corresponding core material, the intersection of these curves is unique and defines the ICB. In case the core is S rich, this intersection may not be unique and Fe-snow zones will form [e.g., *Chen et al.*, 2008].

To model the consequences of such snow zones for the temperature curve, *Dumberry and Rivoldini* [2014] defined the temperature curve equal to the local melting curve in the Fe-snow zone. But given that the Fe-snow process additionally results in a compositional gradient, the melting temperature at a given radius is difficult to determine. Because it is not the scope of this paper to examine thermodynamic constraints on the ICB, nor to discuss the most feasible temperature profile in detail, we choose not to relate the ICB to the modeled temperature profile. Instead, we adopt a similar procedure to *Harder and Schubert* [2001] and *Hauck et al.* [2007, 2013] by varying the ICB independent of the temperature profile in the liquid core (which we assume adiabatic) at the expense of a temperature inconsistency with respect to the local melting temperature. The merits and shortfalls of this approach in terms of errors in density profiles will be addressed in section 4.

The adiabatic temperature profile is obtained by integration of the adiabatic relation

$$\frac{dT}{dP} = \frac{\alpha_r T(r)}{\rho C_p}, \quad (5)$$

with $T(r)$ the local temperature, C_p the material's thermal heat capacity, set at $825 \text{ J K}^{-1} \text{ kg}^{-1}$ [Beutl et al., 1994], and α_r the local thermal expansion coefficient given by

$$\alpha_r = \alpha K \left(\rho \frac{dP}{d\rho} \right)^{-1}. \quad (6)$$

Mercury's solid inner core, if present, may either be conductive or convective. Results in *Rivoldini et al.* [2009] suggest that both assumptions yield similar results. In this paper we assume an isothermal temperature profile for the inner core, similar to *Hauck et al.* [2007, 2013].

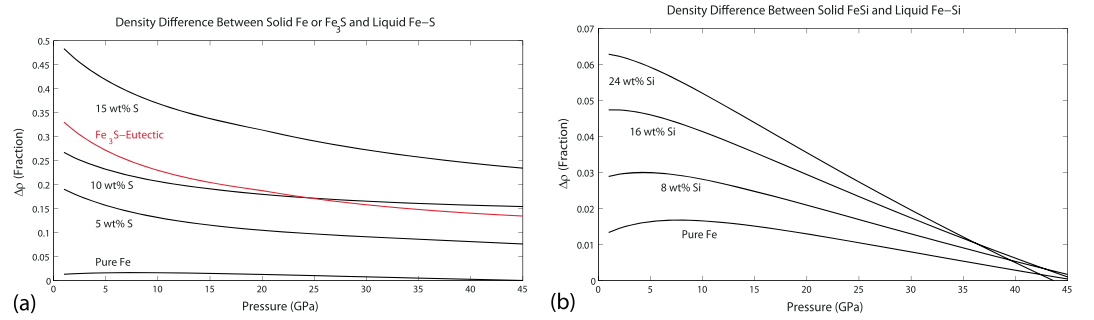


Figure 1. The fractional density difference (a) between solid Fe or Fe₃S and liquid Fe-S and (b) between solid and liquid for solid FeSi and liquid Fe-Si according to the Birch-Murnaghan EOS (equation (1) and Table 2) along the melting curve of corresponding compositions. Note the different scale on the y axis for Figures 1a and 1b.

By iteratively solving equations (1)–(6), we obtain a self-consistent set of gravity, pressure, density, and temperature profiles for any interior configuration model. For each profile set consistent with Mercury's total mass (we allow a deviation of $\pm 0.2\%$ with respect to Mercury's total mass), we calculate the polar moment of inertia C by

$$C = \frac{8\pi}{3} \int_0^R \rho(r) r^4 dr. \quad (7)$$

The polar moment of inertia corresponding to the outer solid shell (C_m) is calculated by equation (7) with the outer liquid boundary (OLB), which is identical to the CMB in Fe-S and Fe-Si models and identical to the base of the FeS layer for the Fe-Si-FeS model, as the lower boundary for the integral. After calculating C and C_m , the normalized polar moment of inertia C/MR^2 and the fraction of it corresponding to the outer solid shell C_m/C are easily derived.

As a goodness of fit statistic with respect to the moment of inertia parameters we calculate the root of the weighted sum over squared deviations of our calculated C/MR^2 and C_m/C with respect to the observed values, with weights reciprocal to their squared standard deviations, given by

$$E_{WSS} = \sqrt{\left(\frac{x - X}{\sigma(x)} \right)^2 + \left(\frac{y - Y}{\sigma(y)} \right)^2}, \quad (8)$$

with x, y the C/MR^2 and C_m/C calculated from density profiles and X, Y the observed central values of C/MR^2 and C_m/C , 0.349 and 0.424, respectively, with standard errors $\sigma(x)$ and $\sigma(y)$ of 0.014 and 0.024 [Mazarico et al., 2014]. This one-dimensional measure for the system's deviation from both planetary moment parameters is useful for presentation purposes and is instrumental to infer the goodness of fit of a given density profile with respect to C/MR^2 and C_m/C . In this procedure the possible overestimation of C_m/C for Mercury of maximum 5% for large inner cores according to Van Hoolst et al. [2012] and Dumberry et al. [2013] is neglected because it is small.

2.4. Planetary Contraction

Usually, core solidification induced radial planetary contraction (ΔR_{cs}) is calculated based on the assumption that the density jump upon solidification ($\Delta\rho$) is constant in case the liquid and solid are of similar composition. For Mercury, $\Delta\rho$ of 5% [e.g., Hauck et al., 2004], 3.5% [Van Hoolst and Jacobs, 2003; Grott et al., 2011], and $\sim 1\%$ [Schubert et al., 1988] have been assumed in the past. Often, ΔR_{cs} is estimated based on the simplifying assumption that the composition of the liquid and solid is similar throughout the core solidification process. In such analyses, ΔR_{cs} estimates are proportional to $\Delta\rho$. In reality, $\Delta\rho$ is not a constant: it varies with pressure and composition. Van Hoolst and Jacobs [2003] and Grott et al. [2011] take the effect of the compositional difference between liquid and solid into account by considering the preferential fractionation on S in the liquid during the solidification of an inner core. The effect of pressure on $\Delta\rho$ has not been included yet. In this study, $\Delta\rho$ is parametrized as the fractional difference between densities of the crystallizing solid and the initial liquid according to their EOSs, which are evaluated along the corresponding pressure profile (P) and the corresponding melting temperature (T_m , to be defined later). The obtained $\Delta\rho$ is plotted as a function of pressure in Figure 1 for several relevant compositions of the solid and liquid. Note that the obtained $\Delta\rho$ that

corresponds to the solidification of Fe_3S (between 12% and 25%) is significantly higher than any previously assumed constant [e.g., *Van Hoolst and Jacobs, 2003; Grott et al., 2011*]. For each generated set of profiles, the volume of contraction (V_C) is calculated by

$$V_C = \int_0^{R_{IC}} 4\pi r^2 \cdot \Delta\rho(r) dr, \quad (9)$$

with $\Delta\rho$ the density jump upon solidification given by

$$\Delta\rho(r) = \frac{\rho_s(r, c_s(r)) - \rho_l(r, c_l(r))}{\rho_l(r, c_l(r))},$$

where ρ_s and ρ_l represent the density of the crystallizing solid and the coexisting liquid given their respective composition c_s and c_l at radius r in terms of light element content (in wt %). ρ_s and ρ_l are parametrized as a solution of the EOS equation (1)

$$\rho_{s,l}(r, c_{s,l}) = \text{EOS}\{P(r), T_m(P(r), c_l(r)), c_{s,l}(r)\},$$

with melting temperature T_m for the light element content of the liquid composition c_l evaluated at a pressure P , which is given by the pressure profile (equation (4)), and c_s the light element content of the precipitating solid.

In the Fe-Si model, c_s and c_l are constant during core solidification. For the Fe-S model, the liquid outer core enriches in S as long as a solid core of pure Fe forms. As a result, c_l varies upon solidification by

$$c_l(r) = \frac{c_B}{\left(1 - \frac{M(r)}{M(r_{\text{cmb}})}\right)}, \quad r \in [0, \min(R_{\text{ICB}}, R_{\text{Fe3S}})],$$

with c_B the S content of the bulk core and $M(r)$ the planetary mass interior to radius r given by the mass profile (equation (2)).

Contrary to the increasing density jump that increases the contraction for the Fe-S model, the liquid core volume expands as its S content increases. This volumetric expansion (V_E) is given by

$$V_E = \int_{R_{\text{IC}}}^{R_{\text{CMB}}} 4\pi r^2 \cdot \Delta q(r) dr, \quad (10)$$

with Δq the density difference between liquid of the bulk core composition and that of the residual liquid, approximated by

$$\Delta q(r) = \frac{\rho_l(r, c_B(r)) - \rho_l(r, c_L(r))}{\rho_l(r, c_L(r))},$$

with ρ_l determined as a solution of the EOS equation (1)

$$\rho_l = \text{EOS}\{P(r), T_m(P(r), c_L), c_{B,L}\},$$

with melting temperature T_m evaluated at pressure P (given by the generated pressure profile) and c_B and c_L the light element content of the bulk core and that of the residual liquid, respectively. Finally, the radial planetary contraction (ΔR_{CS}) is calculated by

$$\Delta R_{\text{CS}} = \frac{V_C - V_E}{4\pi R^2}. \quad (11)$$

For the melting curve of pure Fe-S alloys we apply the parametrization of *Dumberry and Rivoldini [2014]*, which is a slightly altered version of that in *Rivoldini et al. [2011]*, based on experimental melting data and curve fitting from *Brett and Bell [1969]*, *Boehler et al. [1990]*, *Boehler [1993]*, *Shen et al. [1998]*, *Fei et al. [2000]*, *Li et al. [2001]*, *Stewart et al. [2007]*, *Chudinovskikh and Boehler [2007]*, *Chen et al. [2008]*, *Morard et al. [2008]*, and *Anzellini et al. [2013]*. For Fe-Si alloys the melting temperature is linearly interpolated between the pure Fe melting curve and the melting curve of Fe-Si eutectic. For completeness, we provide the parametrization of the melting curve (T_m):

$$T_m(P, \chi_S, \chi_{\text{Si}}) = T_{m,\text{Fe}}(P) - \frac{T_{m,\text{Fe}}(P) - T_{\text{es}}(P)}{\chi_{\text{es}}} \chi_S - \frac{T_{m,\text{Fe}} - T_{\text{esi}}}{\chi_{\text{esi}}} \chi_{\text{Si}},$$

where χ with subscripts S or Si denotes the concentration of S or Si of the liquid and with subscripts e_S or e_{Si} it denotes the S or Si concentration at the eutectic of the corresponding binary Fe-S or Fe-Si system. The melting temperature of Fe is parametrized by

$$T_{m,Fe}(P) = a_1(P_0 + P)^{a_2},$$

where $a_1 = 495.5 \text{ K GPa}^{-a_2}$, $a_2 = 0.42$, and $P_0 = 22.2 \text{ GPa}$. The Fe-S eutectic composition and the melting temperature of the Fe-S eutectic are parametrized as functions of pressure by

$$T_{eS}(P) = \begin{cases} 1265 \text{ K} - 11.15 \frac{K}{\text{GPa}(P - 3 \text{ GPa})}, & \text{for } 3 \text{ GPa} \leq P < 14 \text{ GPa} \\ 1143 \text{ K} + 29 \frac{K}{\text{GPa}(P - 14 \text{ GPa})}, & \text{for } 14 \text{ GPa} \leq P < 21 \text{ GPa} \\ 1346 \text{ K} + 13 \frac{K}{\text{GPa}(P - 21 \text{ GPa})}, & \text{for } 21 \text{ GPa} \leq P < 60 \text{ GPa} \end{cases}$$

and

$$\chi_{eS}(P) = 0.11 + 0.187 \exp\left(-\frac{0.065 P}{\text{GPa}}\right).$$

For more information on the Fe-S melting curve we refer to *Dumberry and Rivoldini* [2014] and *Rivoldini et al.* [2011].

Based on melting experiments at 21 GPa [*Kuwayama and Hirose*, 2004], we set the Fe-Si eutectic composition (χ_{eSi}) at 0.26 wt % Si and the offset of the corresponding melting temperature with respect to the melting curve of pure Fe ($T_{m,Fe} - T_{eSi}$) at 400 K. We note that there is a general lack of experimental data on the melting curve in the Fe-Si system. For this reason, we are unable to parametrize the pressure dependence of $T_{m,Fe} - T_{eSi}$.

The above method to calculate ΔR_{cs} is not suited to quantify the amount of contraction related to solidification of an outer solid FeS layer, because the Fe-Si-FeS models assume a nonhomogeneous liquid core in terms of composition just after core-mantle segregation. The liquid composition from which FeS solidifies is poorly constrained to S rich compared to the Fe-FeS eutectic. Additionally, the large uncertainty in the density of FeS V (discussed in section 2.2) propagates to a large uncertainty in the calculation of the density jump upon solidification ($\Delta\rho$). For these reasons, we do not estimate the amount of contraction or expansion that may result from solidification of an FeS layer.

3. Results

For each interior configuration model we have generated over 2000 profile sets consistent with Mercury's total planetary mass to within $\pm 0.2\%$. Figure 2 shows the radius and pressure of the core-mantle boundary (CMB) and, for the Fe-Si-FeS models, that of the outer liquid boundary (OLB) for these profiles plotted against the deviation of corresponding C/MR^2 and C_m/C with respect to the observed values for Mercury according to *Mazarico et al.* [2014], in terms of propagated standard errors (E_{WSS} ; see equation (8)). Instances of Fe-S and Fe-Si models corresponding to 1 E_{WSS} or lower have CMB radii between 1985 km and 2090 km and 1985 km and 2078 km, respectively, in which CMB radius increases with increasing S and Si concentrations. For the Fe-Si-FeS model, solutions with $E_{WSS} < 1$ have OLB radii between 1990 km and 2090 km, which correlate positively with CMB radii ranging 1995–2276 km. These results set the broadest range for the CMB depth in Mercury today at 164–455 km below the surface, whereas only CMB depths in the range 350–455 km are feasible in the absence of an FeS layer. The relation of Si core contents to the OLB in Fe-Si-FeS model, not shown in Figure 2, is similar to their relation to the CMB in the Fe-Si model. Although solutions consistent with Mercury's total mass yield CMB pressures between 3.4 GPa and 9 GPa for Fe-S and Fe-Si models, instances with $E_{WSS} < 1$ are constrained to 4.6–5.5 GPa and 4.7–5.4 GPa, respectively (Figures 2d and 2e). High CMB pressures correspond to profiles with high average mantle density. For the Fe-Si-FeS model, the OLB pressures constrained by $E_{WSS} < 1$ vary between 4.9 GPa and 5.9 GPa and correspond to CMB pressures ranging 1.8–5.5 GPa, respectively (Figure 2f).

Figure 3 shows the volumetric contraction and expansion (V_C and V_E) by core solidification as estimated by equations (9) and (10) for the Fe-S model and the resulting radial planetary contraction (ΔR_{cs}) calculated

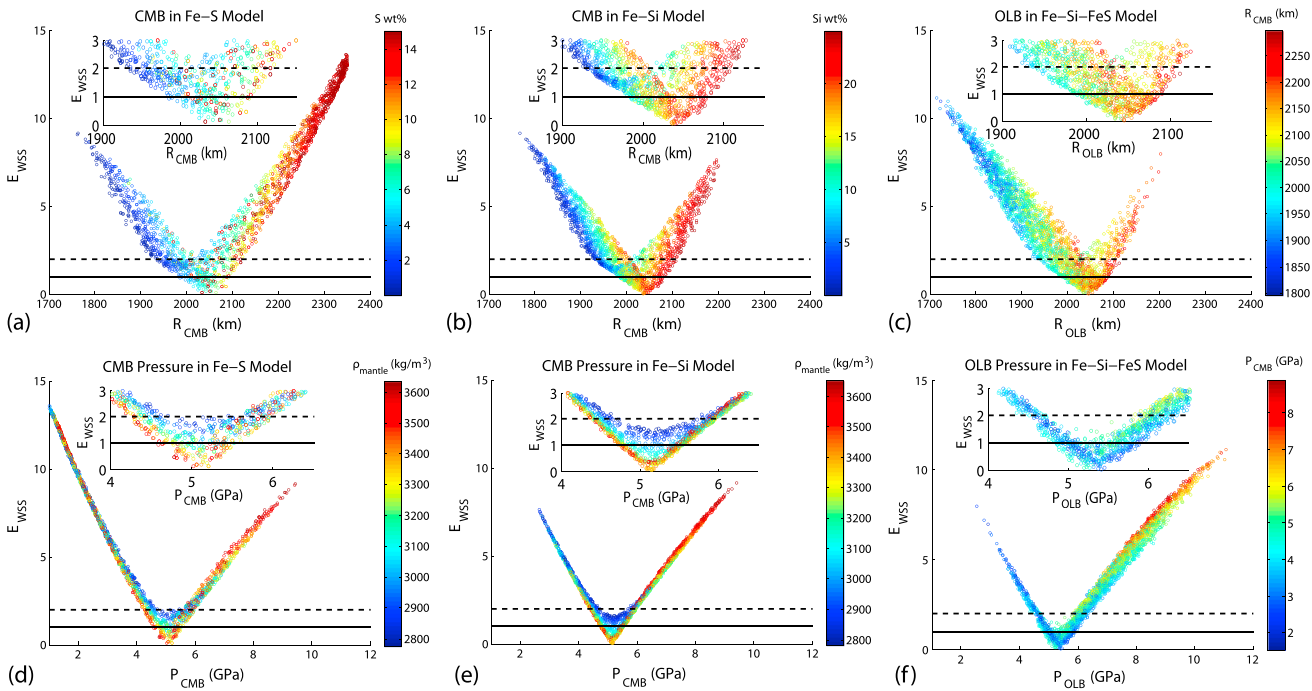


Figure 2. (a and b) The core-mantle boundary radius (R_{CMB}) for solutions of the Fe-S and Fe-Si models, respectively. Colors indicate the total core weight percentage of Si and S for these profiles. (c) The outer liquid boundary radius (R_{OLB}) for solutions of the Fe-Si-FeS model. The colors indicate the CMB radius. (d and e) The CMB pressures for solutions of the Fe-S and Fe-Si models, respectively. Colors indicate the average mantle density. (f) The OLB pressures of profiles for the Fe-Si-FeS model. The results are set out against the standardized error (E_{WSS}) (see equation (8)). Solid and the dashed lines correspond to 1 and 2 standard deviations, respectively, from the moment of inertia parameters. All corresponding solutions are consistent with Mercury's total mass up to 0.2%. The small plots are zoomed in versions of the general plots.

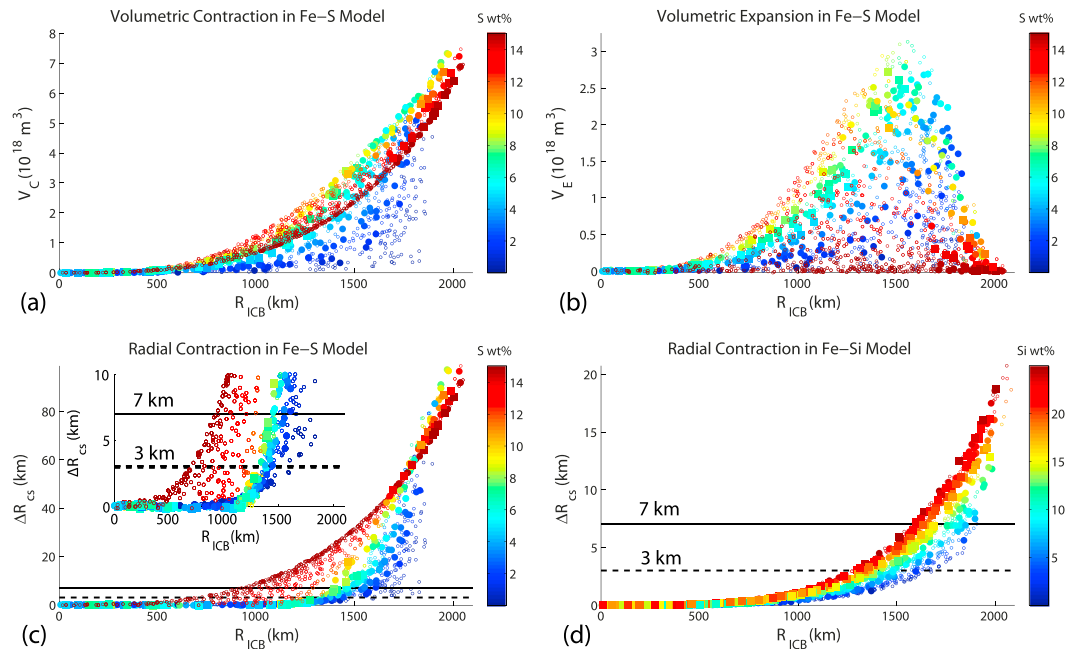


Figure 3. (a) The volumetric contraction induced by core solidification calculated by integrating the density jump upon solidification for the Fe-S model (equation (9)). (b) The volumetric expansion of the residual liquid due to the enrichment of S as Fe-core solidifies (equation (10)). (c and d) The total radial contraction (equation (11)) due to core solidification for the Fe-S and Fe-Si models, respectively. The solid and the dashed lines correspond to the radial contraction of 7 km from Byrne *et al.* [2014] and a contraction of 3 km that incorporates 4 km thermal contraction [Grott *et al.*, 2011; Tosi *et al.*, 2013]. The small plots are zoomed in versions of the general plots. Colors indicate the S (Figures 3a–3c) and Si (Figure 3d) contents in the total core. Filled enlarged squares and circles denote solutions below 1 E_{WSS} and below 2 E_{WSS} , respectively (see Figure 2).

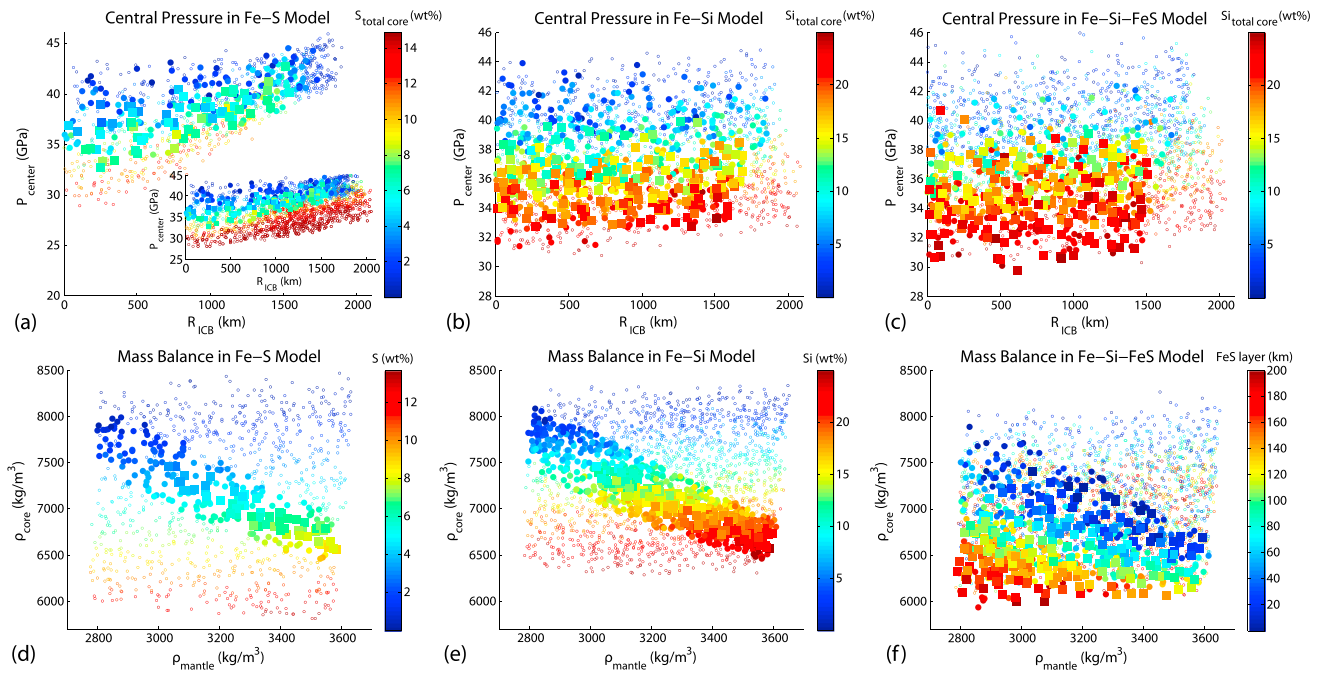


Figure 4. (a–c) The central pressures for Mercury are plotted against the radius of the ICB. (d–f) The average core density plotted against the average mantle density for the Fe–S, Fe–Si, or Fe–Si–FeS model, respectively. Colors indicate the S in the total core (Figures 4a and 4d), the Si contents in the total core (Figures 4d, 4c, and 4e), or the thickness of the FeS layer (Figure 4f). Filled enlarged squares and circles denote solutions below $1 E_{WSS}$ and below $2 E_{WSS}$, respectively, and correspond to a contraction below 7 km in radius (see Figures 2 and 3).

by equation (11) for both the Fe–S and Fe–Si models. Because core solidification in the Fe–Si model does not imply compositional mixing, V_E equals zero and V_C simply equals ΔR_{CS} times the total area of Mercury's surface, by equation (11). For Fe–S models, V_C is generally large for high S contents, as a direct result of the large density jump in those instances (Figure 1). For cores that contain approximately 15 wt % S, V_C is slightly smaller compared to cores with lower S concentrations. This is a direct consequence of the lower density of the Fe_3S phase, which solidifies in these instances, with respect to pure Fe and the corresponding lower density jump (Figure 1).

V_E is generally large for intermediate S contents because at low S contents enrichment of the liquid in S is small, and at high bulk core S contents the composition of the liquid will hit the eutectic (15 wt % S) early on in the solidification process, leading to crystallization of Fe_3S which has a composition close to that of the liquid. ΔR_{CS} is generally high for large inner cores and high S contents. However, most profiles with high bulk core S contents are not consistent with known values for C/MR^2 and C_m/C . For solutions with $E_{WSS} < 1$, the profile with the smallest inner core exceeding the 7 km contraction constraint has an ICB at 1454 km in radius and a bulk core S content of 8.2%. For smaller S content, ΔR_{CS} remains below 7 km for significantly larger cores. The largest inner core constrained by $E_{WSS} < 1$ and $\Delta R_{CS} < 7$ km is 1543 km in radius and has bulk core S contents of 4 wt %. Similar to the Fe–S model, ΔR_{CS} increases with Si content. For solutions with $E_{WSS} < 1$, the smallest core exceeding 7 km contraction has a radius of 1601 km and a Si core content of 24 wt %. The largest inner core that satisfies both $E_{WSS} < 1$ and $\Delta R_{CS} < 7$ km in the Fe–Si model is 1690 km in radius and corresponds to a Si core content of 14 wt %. If we relax the moment of inertia constraint to $E_{WSS} < 2$, inner cores up to 1850 km with 4 wt % Si can be found consistent with $\Delta R_{CS} < 7$.

The central pressure of the planet varies between 32 GPa and 44 GPa for the Fe–S model, between 32 GPa and 40 GPa for the Fe–Si model, and between 29 GPa and 40 GPa for the Fe–Si–FeS model (Figures 4a–4c). High Si and S core content (i.e., a low average core density) lowers the central pressure for all models, whereas the size of the inner core only affects the central pressure in case of S-rich cores; a large pure-Fe inner core increases the central pressure in this model. The insert in Figure 4a shows all solutions of the Fe–S model, whereas the S enrich profiles that result in an Fe_3S inner core layer are left out of the general plot of Figure 4a. None of the solutions with an Fe_3S phase meet the constraints set by C/MR^2 , C_m/C , and the

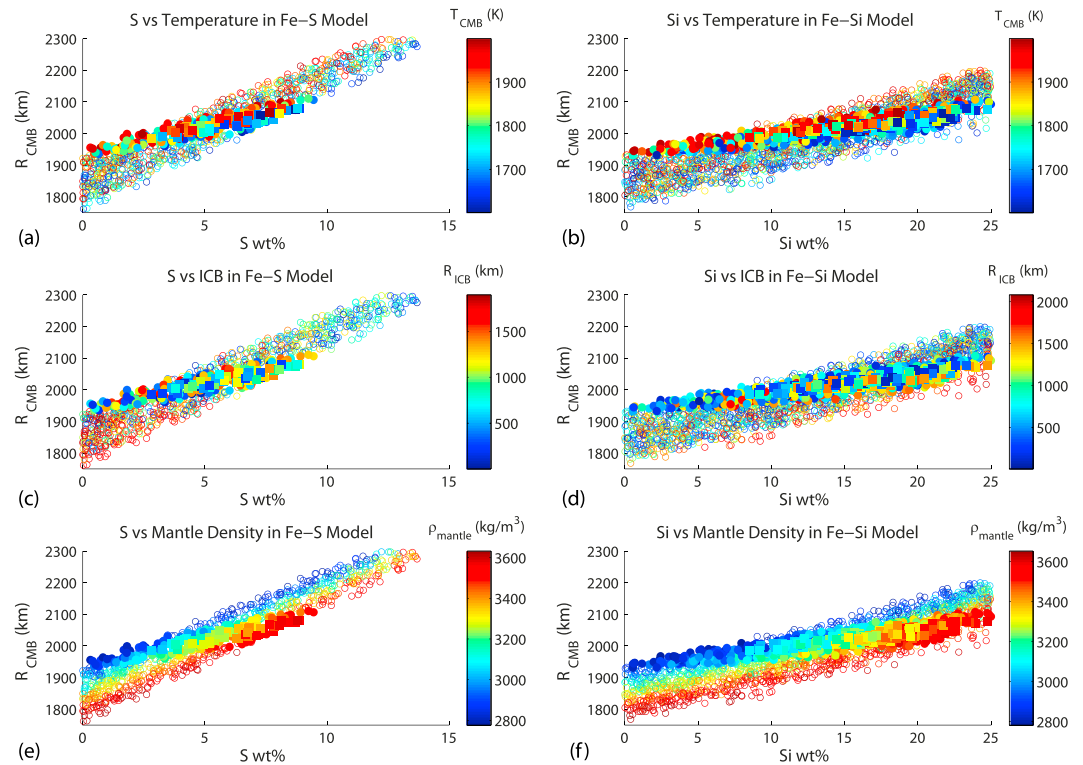


Figure 5. These plots show the relation between the CMB and S and Si total core content for the Fe-S and Fe-Si models, respectively. Colors correspond to values of (a and b) the CMB temperature, (c and d) the inner core boundary (R_{ICB}), and (e and f) the average mantle density. Filled enlarged squares and circles denote solution below $1 E_{WSS}$ and below $2 E_{WSS}$, respectively, and correspond to a contraction below 7 km in radius (see Figures 2 and 3).

maximum of 7 km planetary contraction simultaneously. We conclude that the Fe_3S layer does not provide a feasible configuration and the results with an Fe_3S phase are therefore left out for the remainder of this paper. Figures 4d and 4e show that there is a typical trade-off between the average density of the core and that of the mantle in configurations that meet the constraints set by C/MR^2 and C_m/C . For both the Fe-S and Fe-Si models, the average core and mantle densities are within $6500\text{--}7500\text{ kg m}^{-3}$ and $3000\text{--}3600\text{ kg m}^{-3}$, respectively, if we only consider models that satisfy $E_{WSS} < 1$. If we relax the moment of inertia constraints to $E_{WSS} < 2$, we find solutions with average core up to 8000 kg m^{-3} and average mantle densities down to 2800 kg m^{-3} . For the Fe-Si-FeS model (Figure 4f), the same upper density limits apply but no lower boundaries for the average density of the core or of the mantle seem to exist within the ranges examined in this paper. This result is due to the high density for solid FeS with respect to the silicate mantle that attributes to the moment of inertia of the outer solid shell. Therefore, the presence of a large FeS layer requires a low average mantle and low core density in order to remain consistent with C_m/C and C/MR^2 .

The relation between core composition and CMB radius for results of the Fe-S and Fe-Si models is presented in Figure 5 with colors to indicate either the assumed CMB temperature, the inner core radius (R_{ICB}), or the average density of the mantle. The S content of Mercury's total core is constrained to 2.8–8.9 wt %, and the Si content is constrained to above ~ 8.5 wt % by $E_{WSS} < 1$ and $\Delta R_{CS} < 7$ km for the Fe-S and Fe-Si models, respectively. The effect of CMB temperature on the CMB radius is identified but small, as we notice that the correspondence between high CMB radii and high CMB temperatures and the correspondence between low CMB radii and low CMB temperatures are barely observed through the noise in colors (Figures 5a and 5b). The size of the inner core plays a role in the Fe-S model, where large core sizes are allowed only for low S contents and small CMB radii, whereas the inner core size has little effect in the Fe-Si model. The variables that dominate the variability in CMB radius are the abundance of light elements in the core and the averaged mantle density. Higher mantle densities relate to a larger core and more light elements in the core, whereas solutions with low average mantle densities correspond to smaller cores that mainly consist of Fe.

4. Discussion

4.1. Error Propagation

All profile sets used for this study are self-consistent in terms of mass, gravity, pressure, density, and temperature and agree with Mercury's total mass to within 0.2%. The density profiles and planetary contraction estimates calculated in this study depend largely on the EOS parameters that characterize the density of the corresponding materials. The accuracy of these EOS parameters determines the accuracy of the results in this study. Generally, densities of solid phases are known more accurately compared to those of liquid phases because their unit cell volumes can be studied with relatively high precision by in situ diffraction measurements up to pressures exceeding the range relevant for Mercury. Densities of all solids in this study (HCP Fe, FeS V, FeSi, and Fe₃S) have been studied across the entire pressure regime for which they are applied here (<45 GPa), whereas the densities of liquid alloys are mostly extrapolated from EOSs derived from experiments at lower pressures. The uncertainties in solid and liquid densities are often assumed to be around 1% and 2.5%, respectively [e.g., *Kaiura and Toguri*, 1979; *Sanloup et al.*, 2000; *Hauck et al.*, 2007, 2013]. In many modeling studies, however, only the best fit EOS is implemented, neglecting these errors. The method applied in this study, which is similar to that in, e.g., *Harder* [1998], *Harder and Schubert* [2001], and *Hauck et al.* [2007, 2013], has a temperature inconsistency at the ICB with respect to the local melting temperature and differs from, e.g., *Rivoldini et al.* [2009], *Rivoldini and van Hoolst* [2013], and *Dumberry and Rivoldini* [2014] on this issue. By varying the ICB and T_{CMB} independently within ranges given in Table 1, largest local temperature inconsistencies are ~500 K. Although this is rather large from a thermodynamic point of view, the density variations resulting from this offset are at most $\pm 2\%$ and are of the same order as the errors on EOS parameters. Given that it is not the scope of this paper to examine whether there exists a feasible temperature profile that corresponds with the location of the ICB, the variable local temperature offset results in an error that is not larger than the error propagation in the bulk set of density profiles. Additional error propagation for the density of solid FeS V is provided by varying the corresponding reference density by $\pm 2\%$.

Small inaccuracies of a few percent could, however, substantially affect the obtained estimates for planetary contraction since these estimates are mainly sensitive to density differences that are on the order of a few percent, as parametrized by the EOSs (Figure 1). However, these planetary contraction estimates are derived from the density differences between solid and liquid phases, implying that only internal consistency of the applied EOSs is required to yield reliable results. We argue that these uncertainties are minimized by carefully selecting an internally consistent set of EOSs and by evaluating the density jump at melting temperatures corresponding to the respective composition. For instance, the quadratic relation of the bulk modulus for Fe-S liquid with S content as determined by *Sanloup et al.* [2000] fits the 0 wt % S (pure Fe) EOS of *Anderson and Ahrens* [1994] remarkably well when the latter is transformed to the here applied equivalent isothermal bulk modulus [*Balog et al.*, 2003]. The same applies to the linear relation of Fe-Si liquids bulk modulus with Si content [*Sanloup et al.*, 2004]. The difference between liquid and solid of equal compositions for pressures relevant for most core material is between 1% and 6% for pure Fe and Fe-24 wt % Si, respectively (Figure 1b), which is in the range of previously applied constant values for $\Delta\rho$ [*Schubert et al.*, 1988; *Van Hoolst et al.*, 2007; *Grott et al.*, 2011]. For Fe₃S and liquid of similar composition $\Delta\rho$ takes values of around 20% at high pressure, which is significantly larger than the value assumed by *Van Hoolst and Jacobs* [2003] but does induce an expected downward jump in $\Delta\rho$ when the liquid of Fe-S composition reaches the eutectic during solidification of a pure Fe inner core (Figure 1a). We argue that more accurate EOSs would increase the robustness of our results and may resolve the discrepancy in the values that are used for $\Delta\rho$ throughout various studies.

4.2. Comparison With Previous Studies

The ranges presented here for OLB radii (1985–2090 km) are broadly consistent with those obtained by *Rivoldini and Van Hoolst* [2013] (1965–2043 km) and *Hauck et al.* [2013] (1990–2050), as is the trend toward larger R_{CMB} for higher concentrations of light elements for the core and higher average mantle densities. The reason for obtaining an upper limit for OLB radius of 2090 km, i.e., higher than that of *Hauck et al.* [2013] and *Rivoldini and Van Hoolst* [2013], is likely a result of the slightly lower C_{m}/C of *Mazarico et al.* [2014] that is adopted in this study compared to that of *Margot et al.* [2012] that was adopted in the other studies. The range of core S contents constrained to 2.8–8.9 wt % by C/MR^2 and C_{m}/C for the Fe-S model implies that the presence of Fe₃S in Mercury's core is impossible assuming a binary Fe-S core. This range is larger than the range deduced by *Rivoldini and Van Hoolst* [2013] that constrains the S content to 4.5 ± 1.8 wt %. The main reason for this

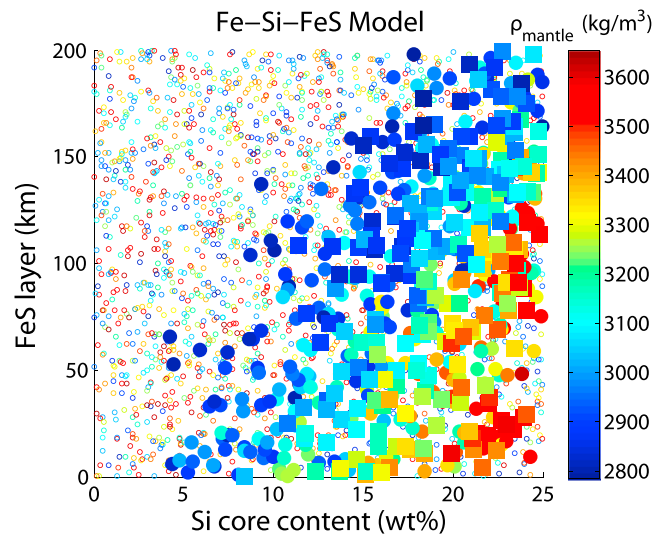


Figure 6. In this figure the thickness of the FeS layer has been plotted against the Si content corresponding to the core below the FeS layer for solutions of the Fe-Si-FeS model. Colors indicate the corresponding averaged mantle density. Filled enlarged squares and circles denote solution below 1 E_{WSS} and below 2 E_{WSS} , respectively, and correspond to a contraction below 7 km in radius (see Figures 2 and 3).

$6980 \pm 280 \text{ kg m}^{-3}$. Our results show that there is a typical trade-off between the average mantle and core densities that slightly influences the location of the CMB (Figures 4 and 5). Additionally, we observe that a large FeS layer relates to low average mantle densities (Figure 6). This is consistent with Hauck et al. [2013, Figure 11].

Regarding solutions of the Fe-S and Fe-Si models, relating the planetary contraction estimates to the maximum radial contraction of 7 km given by Byrne et al. [2014] has constrained the inner core size for instances with high S (~8.9 wt %) or Si (~25 wt %) contents down to a radius of 1454 km and 1543 km, respectively (Figure 3), whereas cores of low Si or S contents would allow inner cores to solidify up to 1690 km in radius. Dumberry and Rivoldini [2014] concluded that the size of an inner core for the Fe-S model is likely constrained to a maximum radius of 1325 ± 250 km based on thermodynamic arguments and taking the presence of snow zones into account. No equivalent claim can be made based on our results regarding the planetary contraction limit of 7 km by Byrne et al. [2014]. However, thermal expansion/contraction, partial melting, and differentiation of a cooling planet substantially affect the overall planetary contraction. Grott et al. [2011] and Tosi et al. [2013] most recently estimated the net contribution of mantle differentiation and the thermal contraction of Mercury as a whole on radial planetary contraction in the range of 2–4 km in radius. Additionally, total global contraction estimates down to 3.1 km have been given in Byrne et al. [2014]. Consequently, the upper limit for ΔR_{cs} in this study may be substantially lowered. Using a contraction of 3 km (obtained by subtracting the maximum 4 km thermal contraction from the 7 km total contraction observation by Byrne et al. [2014]) as upper limit for ΔR_{cs} would, for example, constrain the size of the inner core to a maximum radius of 1274 km for bulk core compositions near 8.9 wt % and 1300 km for a bulk core of approximately 25 wt % Si. Inner cores for a core low in light elements (~2.8 wt % S or ~8.5 wt % Si) ranging up to 1380 km in radius are found consistent with $\Delta R_{cs} < 3$ km.

4.3. The Evolution of a Solid FeS Layer

The presence of a solid FeS layer has important implications for the current thermal state and evolution of Mercury, given the FeS melting temperature [e.g., Tosi et al., 2013; Michel et al., 2013], and would lower the size of silicate mantle significantly [e.g., Smith et al., 2012; Hauck et al., 2013] (Figure 2). The latter has large implications for studies that focus on the mineralogical makeup and dynamics of Mercury's mantle [e.g., Brown and Elkins-Tanton, 2009; Verhoeven et al., 2009; Vander Kaaden and McCubbin, 2015]. For this

discrepancy is that they varied the mantle densities within the range $3300 \pm 200 \text{ kg m}^{-3}$, whereas we explored a larger range of $3200 \pm 400 \text{ kg m}^{-3}$. Additionally, the variability in temperature profiles provides some error propagation of applied EOSs. These differences in methodology broaden the feasible solution space and specifically the range of S content that is found consistent with C/MR^2 and C_m/C (Figure 5e). The Si content of a binary Fe-Si core is constrained to above 8.5 wt %, but in case of an FeS layer attached to the base of the mantle the minimum Si content increases with the size of such a layer to 20 wt % Si for an FeS layer of 200 km thickness (Figure 6). The range of average core densities consistent with C/MR^2 and C_m/C of $7000 \pm 500 \text{ kg m}^{-3}$ spans the ranges of both Rivoldini and Van Hoolst [2013] and Hauck et al. [2013] of, respectively, $7233 \pm 267 \text{ kg m}^{-3}$ and

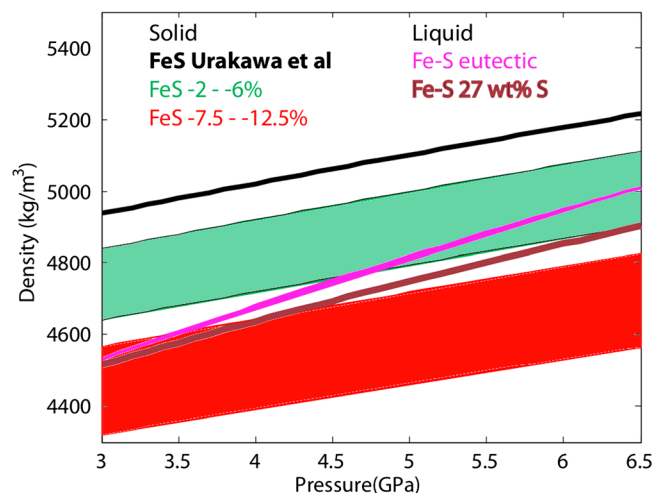


Figure 7. This plot shows density curves of solid FeS and liquid Fe-S at 1400 K: The black curve shows the FeS V (HPP) EOS from *Urakawa et al.* [2004], the green area shows the range of densities for solid FeS applied in this study, the red area shows the range of densities for solid FeS applied in *Hauck et al.* [2013], the purple curve shows the density of the liquid Fe-S for the eutectic composition at corresponding pressure, and the brown curve shows the density of liquid Fe-S for 27 wt % S. The applied liquid EOS parameters are given in Table 2 and are based on *Sanloup et al.* [2000] and *Jing et al.* [2014].

reason it is of interest to discuss the likelihood of such a configuration. The configuration was first proposed in *Smith et al.* [2012] and *Hauck et al.* [2013] based on the assumption that solid FeS, which may precipitate at the outer core, is less dense than the surrounding Fe-S liquid, although the liquid is required to be S rich compared to the eutectic composition. In *Hauck et al.* [2013], the density of solid FeS V at pressures corresponding to the lower outer solid shell (between 3 GPa and 6 GPa) varies between 7.5% and 12.5% below the EOS for FeS V (HPP) as published in *Urakawa et al.* [2004], which fits FeS V densities at higher pressures (above ~11 GPa). We have argued in section 2.2 that this density offset is more likely in the range of 2–6%. Figure 7 compares the density ranges of solid FeS V as parametrized by *Hauck et al.* [2013] (red area) and by us (green area) in this study at 1400 K. The density

of liquid Fe-S for the eutectic composition and that of 27 wt % S based on *Sanloup et al.* [2000] and *Jing et al.* [2014] (Table 2) have been plotted as well. Given that a S content of 27 wt % is close to the eutectic for the corresponding pressure regime, the density of the liquid shown in Figure 6 is likely on the high end and will further decrease for higher S contents. Figure 7 shows clearly that the density of solid FeS according to the EOS applied in our study is higher than that of liquid Fe-S for the eutectic composition. We argue based on Figure 7 that it is doubtful that solid FeS will float upon crystallization at the outer core of Mercury. Solid FeS may well sink to greater depth instead. This indicates that a solid FeS layer attached to the mantle may be unlikely and an alternative mechanism would be required to have FeS layer located at the top of the outer core. We stress that there are substantial discrepancies in the density of S-rich liquids between recent studies [*Nishida et al.*, 2008, 2011, 2013; *Chen et al.*, 2014; *Jing et al.*, 2014]. In particular, the difference in reference densities that are applied for liquid Fe-S of intermediate S contents (0–36 wt % S) propagates to large diversity of the density of liquid Fe-S at high pressure between different recent studies. Additional high-precision data will be required to further resolve the issue of the buoyancy of an FeS layer in the core of Mercury.

5. Summary and Conclusion

Three end-member interior configuration models with core compositions in a limited part of the Fe-Si-S system for the planet Mercury were examined based on corresponding density profiles, specifically to assess which of these models when accompanied with partial core solidification is consistent with the new limit of 7 km planetary contraction as observed by *Byrne et al.* [2014].

Results indicate that the CMB, or the lower boundary for an FeS layer that has been proposed to reside between mantle and liquid outer core, is between 1985 km and 2090 km in radius, with the high values corresponding to high Si and S contents and high mantle densities or the presence of an FeS layer. The pressure of this boundary is between 4.6 GPa and 5.5 GPa for models without an FeS layer and between 4.9 GPa and 5.9 GPa for models with an FeS layer. A comparison of density data for solid FeS and liquid Fe-S has been performed to examine the capability of FeS to float on liquid Fe-S upon precipitating at the outer core and subsequently accrete to the lower mantle. This comparison shows that it is not at all evident that solid FeS will float but instead may well sink to greater depth. This would imply that a separate mechanism is required

for FeS layer to be located at the top of the outer core. Alternatively, it indicates that the suggested FeS layer is more likely absent. We stress that caution on this point should be made due to large uncertainties in the density of relevant Fe-S liquids.

Considering models without an FeS layer, the S and Si total core contents are constrained to 2.8–8.9 wt % and above 8.5 wt %, respectively, for cores of binary Fe-S or Fe-Si alloys. Results indicate that an FeS layer requires high Si contents in the rest of the core in order to be consistent with the planetary moment parameters. The size of the inner core is constrained by the observed planetary contraction of 7 km [Byrne *et al.*, 2014] to below 1454 km or 1543 km in radius for bulk cores rich in S (~8.9 wt %) or Si (~25 wt %), respectively. For cores low in light elements (~2.8 wt % S or ~8.5 wt % Si), inner cores up to 1960 km may remain consistent with this amount of planetary contraction due to core solidification. If we assume a net contribution of radial contraction by long-term mantle differentiation and thermal cooling of 4 km, inner core sizes are constrained to below 1274 km or 1300 km in radius for bulk cores rich in S (~8.9 wt %) or Si (~25 wt %), respectively, and ~1380 km for cores low in light elements. Such constraints are similar to constraints on the size of the inner core proposed by Dumberry and Rivoldini [2014] based on thermodynamic arguments. We do note that more precise EOSs, more detailed analysis of surface landforms, and a better understanding of Mercury's thermal evolution are necessary to make global contraction constraints on the size of the inner core more robust.

Acknowledgments

This research was funded by a Netherlands Space Office User Support Programme Space Research grant (ALW-GO/12-38) to W.v.W. and the Belgian Science Policy Office (contract BR/143/A2/COME-IN). All data for this paper are properly cited and referred to in the reference list. The numerical output from these equations necessary to generate the figures is available upon request to the corresponding author. We thank M. Dumberry, S. Padovan, and Editor S. Hauck for their constructive comments that have significantly improved the paper.

References

- Anderson, J. D., G. Colombo, P. B. Esposito, E. L. Lau, and G. B. Trager (1987), The mass, gravity field, and ephemeris of Mercury, *Icarus*, 71(3), 337–349, doi:10.1016/0019-1035(87)90033-9.
- Anderson, W. W., and T. J. Ahrens (1994), An equation of state for liquid iron and implications for the Earth's core, *J. Geophys. Res.*, 99(B3), 4273–4284, doi:10.1029/93JB03158.
- Anzellini, S., A. Dewaele, M. Mezouar, P. Loubeyre, and G. Morard (2013), Melting of iron at Earth's inner core boundary based on fast X-ray diffraction, *Science*, 340(6131), 464–466, doi:10.1126/science.1233514.
- Ash, M. E., I. I. Shapiro, and W. B. Smith (1971), The system of planetary masses, *Science*, 174(4009), 551–556, doi:10.1126/science.174.4009.551.
- Balog, P. S., R. A. Secco, D. C. Rubie, and D. J. Frost (2003), Equation of state of liquid Fe-10 wt % S: Implications for the metallic cores of planetary bodies, *J. Geophys. Res.*, 108(B2), 2124, doi:10.1029/2001JB001646.
- Berthet, S., V. Malavergne, and K. Righter (2009), Melting of the Indarch meteorite (EH4 chondrite) at 1 GPa and variable oxygen fugacity: Implications for early planetary differentiation processes, *Geochim. Cosmochim. Acta*, 73(20), 6402–6420, doi:10.1016/j.gca.2009.07.030.
- Beutl, M., G. Pottlacher, and H. Jäger (1994), Thermophysical properties of liquid iron, *Intl. J. Thermophys.*, 15(6), 1323–1331, doi:10.1007/BF01458840.
- Boehler, R. (1993), Temperatures in the Earth's core from melting-point measurements of iron at high static pressures, *Nature*, 363(6429), 534–536, doi:10.1038/36353534a0.
- Boehler, R., N. von Bagen, and A. Chopelas (1990), Melting, thermal expansion, and phase transitions of iron at high pressures, *J. Geophys. Res.*, 95(B13), 21,731–21,736, doi:10.1029/JB095iB13p21731.
- Brett, R., and P. M. Bell (1969), Melting relations in the Fe-rich portion of the system Fe-FeS at 30 kb pressure, *Earth Planet. Sci. Lett.*, 6(6), 479–482, doi:10.1026/0012-821X(69)90119-8.
- Breuer, D., S. A. Hauck II, M. Buske, M. Pauer, and T. Spohn (2007), Interior evolution of Mercury, *Space Sci. Rev.*, 132(2–4), 229–260, doi:10.1007/s11214-007-9228-9.
- Brown, S. M., and L. T. Elkins-Tanton (2009), Compositions of Mercury's earliest crust from magma ocean models, *Earth Planet. Sci. Lett.*, 286(3), 446–455, doi:10.1016/j.epsl.2009.07.010.
- Byrne, P. K., C. Klimczak, A. C. Şengör, S. C. Solomon, T. R. Watters, and S. A. Hauck (2014), Mercury's global contraction much greater than earlier estimates, *Nat. Geosci.*, 7(4), 301–307, doi:10.1038/ngeo2097.
- Chabot, N. L., E. A. Wollack, R. L. Klima, and M. E. Minitti (2014), Experimental constraints on Mercury's core composition, *Earth Planet. Sci. Lett.*, 390, 199–208, doi:10.1016/j.epsl.2014.01.004.
- Chen, B., J. Li, and S. A. Hauck (2008), Non-ideal liquidus curve in the Fe-S system and Mercury's snowing core, *Geophys. Res. Lett.*, 35 L07201, doi:10.1029/2008GL033311.
- Chen, J., T. Yu, S. Huang, J. Girard, and X. Liu (2014), Compressibility of liquid FeS measured using X-ray radiograph imaging, *Phys. Earth Planet. Inter.*, 228, 294–299, doi:10.1016/j.pepi.2013.12.012.
- Chudinovskikh, L., and R. Boehler (2007), Eutectic melting in the system Fe-S to 44 GPa, *Earth Planet. Sci. Lett.*, 257(1–2), 97–103, doi:10.1016/j.epsl.2007.02.024.
- De Jager, C. (1971), Internal constitution and thermal histories of the terrestrial planets, *Inter. Astron. Union*, 2, 204–227, doi:10.1007/978-94-010-3102-8_11.
- Di Achille, G., C. Popa, M. Massironi, E. Mazzotta Epifani, M. Zusi, G. Cremonese, and P. Palumbo (2012), Mercury's radius change estimates revisited using MESSENGER data, *Icarus*, 221(1), 456–460, doi:10.1016/j.icarus.2012.07.005.
- Dombard, A. J., and S. A. Hauck (2008), Despinning plus global contraction and the orientation of lobate scarps on Mercury: Predictions for MESSENGER, *Icarus*, 198(1), 274–276, doi:10.1016/j.icarus.2008.06.008.
- Dumberry, M. (2011), The free librations of Mercury and the size of its inner core, *Geophys. Res. Lett.*, 38 L16202, doi:10.1029/2011GL048277.
- Dumberry, M., and A. Rivoldini (2014), Mercury's inner core size and core-crystallization régime, *Icarus*, 248, 254–268, doi:10.1016/j.icarus.2014.10.038.
- Dumberry, M., A. Rivoldini, T. van Hoolst, and M. Yseboodt (2013), The role of Mercury's core density structure on its longitudinal librations, *Icarus*, 225(1), 62–74, doi:10.1016/j.icarus.2013.03.001.
- Fei, Y., C. T. Prewitt, H. Mao, and C. M. Bertka (1995), Structure and density of FeS at high pressure and high temperature and the internal structure of Mars, *Science*, 268(5219), 1892–1894, doi:10.1126/science.268.5219.1892.

- Fei, Y., J. Li, C. M. Bertka, and C. T. Prewitt (2000), Structure type and bulk modulus of Fe_3S , a new iron-sulfur compound, *Am. Mineral.*, 85(11–12), 1830–1833, doi:10.2138/am-2000-11-1229.
- Grott, M., D. Breuer, and M. Laneuville (2011), Thermo-chemical evolution and global contraction of mercury, *Earth Planet. Sci. Lett.*, 307(1), 135–146, doi:10.1016/j.epsl.2011.04.040.
- Harder, H. (1998), Phase transitions and the three-dimensional planform of thermal convection in the Martian mantle, *J. Geophys. Res.*, 103(E7), 16,775–16,797, doi:10.1029/98JE01543.
- Harder, H., and G. Schubert (2001), Sulfur in Mercury's core?, *Icarus*, 151(1), 118–122, doi:10.1006/icar.2001.6586.
- Hauck, S. A., A. J. Dombard, R. J. Phillips, and S. C. Solomon (2004), Internal and tectonic evolution of Mercury, *Earth Planet. Sci. Lett.*, 222(3), 713–728, doi:10.1016/j.epsl.2004.03.037.
- Hauck, S. A., S. C. Solomon, and D. A. Smith (2007), Predicted recovery of Mercury's internal structure by MESSENGER, *Geophys. Res. Lett.*, 34, L18201, doi:10.1029/2007GL030793.
- Hauck, S. A., et al. (2013), The curious case of Mercury's internal structure, *J. Geophys. Res. Planets*, 118, 1204–1220, doi:10.1002/jgre.20091.
- Hillgren, V., and Y. Fei (2013), Metal-silicate partitioning of Si and S in highly reducing conditions: Implications for the evolutionary history of Mercury, *LPSC Abstr.*, 45, 2751.
- Hixson, R. S., M. A. Winkler, and M. L. Hodgdon (1990), Sound speed and thermophysical properties of liquid iron and nickel, *Phys. Rev.*, B42, 6485–6491, doi:10.1103/PhysRevB.42.6485.
- Jeffreys, H. (1936), The density distributions in the inner planets, *Geophys. J. Inter.*, 4(s1), 62–71, doi:10.1111/j.1365-246x.1937.tb00410.x.
- Jing, Z., Y. Wang, Y. Kono, T. Yu, T. Sakamaki, C. Park, M. L. Rivers, S. R. Sutton, and G. Shen (2014), Sound velocity of Fe-S liquids at high pressure: Implications for the Moon's outer core, *Earth Planet. Sci. Lett.*, 396, 78–87, doi:10.1016/j.epsl.2014.04.015.
- Kaiura, G. H., and J. M. Toguri (1979), Densities of the molten Fe-S, Fe-Cu₂S and Fe-S-O systems—Utilizing a Bottom-Balance Archimedeian Technique, *Can. Metall. Quart.*, 18(2), 155–164, doi:10.1179/cmq.1979.18.2.155.
- Klaassen, K. P. (1975), Mercury rotation period determined from Mariner 10 photography, *J. Geophys. Res.*, 80(17), 2415–2416, doi:10.1029/JB080i017p02415.
- Komabayashi, T., and Y. Fei (2010), Internally consistent thermodynamic database for iron to the Earth's core conditions, *J. Geophys. Res.*, 115, B03202, doi:10.1029/2009JB006442.
- Komabayashi, T., Y. Fei, Y. Meng, and V. Prakapenka (2009), In-situ X-ray diffraction measurements of the γ - ϵ transition boundary of iron in an internally-heated diamond anvil cell, *Earth Planet. Sci. Lett.*, 282(1), 252–257, doi:10.1016/j.epsl.2009.03.025.
- Kuwayama, Y., and K. Hirose (2004), Phase relations in the system Fe-FeSi at 21 GPa, *Am. Mineral.*, 89(2–3), 273–276, doi:10.1016/j.epsl.2013.04.035.
- Levenberg, K. (1944), A method for the solution of certain problems in least squares, *Quart. J. App. Math.*, 2(2), 164–168.
- Li, J., Y. Fei, H. K. Mao, K. Hirose, and S. R. Shieh (2001), Sulfur in the Earth's inner core, *Earth Planet. Sci. Lett.*, 193(3), 509–414, doi:10.1016/S0012-821X(01)00521-0.
- Lin, J. F., A. J. Campbell, D. L. Heinz, and G. Y. Shen (2003), Static compression of iron-silicon alloys: Implications for silicon in the Earth's core, *J. Geophys. Res.*, 108(B1), 2045, doi:10.1029/2002JB001978.
- Lyttleton, R. A. (1969), On the internal structures of Mercury and Venus, *Astrophys. Space Sci.*, 5(1), 18–35, doi:10.1007/BF00653933.
- Macdonald, G. J. F. (1962), On the internal constitution of the inner planets, *J. Geophys. Res.*, 67(7), 2945–2974, doi:10.1029/JZ067i007p02945.
- Malavergne, V., M. J. Toplis, S. Berthet, and J. Jones (2010), Highly reducing conditions during core formation on Mercury: Implications for internal structure and the origin of a magnetic field, *Icarus*, 206(1), 199–209, doi:10.1026/j.icarus.2009.09.001.
- Margot, J. L., S. J. Peale, S. C. Solomon, S. A. Hauck, F. D. Ghigo, R. F. Jurgens, M. Yseboodt, J. D. Giorgini, S. Padovan, and D. B. Campbell (2012), Mercury's moment of inertia from spin and gravity data, *J. Geophys. Res.*, 117, E00L09, doi:10.1029/2012JE004161.
- Margot, J.-L., S. Peale, R. Jurgens, M. Slade, and I. Holin (2007), Large longitude libration of Mercury reveals a molten core, *Science*, 316(5825), 710–714, doi:10.1126/science.1140514.
- Marquardt, D. W. (1963), An algorithm for least-squares estimation of nonlinear parameters, *J. Soc. Ind. Appl. Math.*, 11(2), 431–441, doi:10.1137/0111030.
- Mazarico, E., A. Genova, S. Goossens, F. G. Lemoine, G. E. Neumann, M. T. Zuber, D. E. Smith, and S. C. Solomon (2014), The gravity field, orientation, and ephemeris of Mercury from MESSENGER observations after three years in orbit, *J. Geophys. Res. Planets*, 119, 2417–2436, doi:10.1002/2014JE004675.
- McCoy, T. J., T. L. Dickinson, and G. E. Lofgren (1999), Partial melting of the Indarch (EH4) meteorite: A textural, chemical, and phase relations view of melting and melt migration, *Meteorit. Planet. Sci.*, 34(5), 735–746, doi:10.1111/j.1945-5100.1999.tb01386.x.
- McCubbin, F. M., M. A. Riner, and K. E. Vander Kaaden (2012), Is Mercury a volatile-rich planet?, *Geophys. Res. Lett.*, 39, L09202, doi:10.1029/2012GL051711.
- Michel, N. C., S. A. Hauck, S. C. Solomon, R. J. Phillips, J. H. Roberts, and M. T. Zuber (2013), Thermal evolution of Mercury as constrained by MESSENGER observations, *J. Geophys. Res. Planets*, 118, 1033–1044, doi:10.1002/jgre.20049.
- Morard, G. C., and T. Katsura (2010), Pressure-temperature cartography of Fe-S-Si immiscible system, *Geochim. Cosmochim. Acta*, 74(12), 3659–3667, doi:10.1016/j.gca.2010.03.025.
- Morard, G., C. Sanloup, B. Guillot, G. Fiquet, M. Mezouar, J. P. Perrillat, G. Garbarino, K. Mibe, T. Komabayashi, and K. Funakoshi (2008), In situ structural investigation of Fe-S-Si immiscible liquid system and evolution of Fe-S bond properties with pressure, *J. Geophys. Res.*, 113, B10205, doi:10.1029/2008JB005663.
- Ness, N. F., K. Behannon, R. Lepping, Y. Whang, and K. Schatten (1974), Magnetic field observations near Mercury: Preliminary results from Mariner 10, *Science*, 185(4146), 151–160, doi:10.1126/science.185.4546.151.
- Ness, N. F., K. Behannon, R. Lepping, and Y. Whang (1975), The magnetic field of Mercury, 1, *J. Geophys. Res.*, 80(19), 2708–2716, doi:10.1029/JA080i019p02708.
- Nishida, K., H. Terasaki, E. Ohtani, and A. Suzuki (2008), The effect of sulfur content of the density of liquid Fe-S at high pressure, *Phys. Chem. Mineral.*, 35(7), 417–423, doi:10.1007/s00269-008-0236-4.
- Nishida, K., E. Ohtani, S. Urakawa, A. Suzuki, T. Sakamaki, H. Terasaki, and Y. Katayama (2011), Density measurement of liquid FeS at high pressures using synchrotron X-ray adsorption, *Am. Mineral.*, 96(5–6), 864–868, doi:10.2138/am.2011.3616.
- Nishida, K., Y. Kono, H. Terasaki, S. Takahashi, M. Ishii, Y. Shimoyama, Y. Higo, K.-L. Funakoshi, T. Irifune, and E. Ohtani (2013), Sound velocity measurements in liquid Fe-S at high pressure: Implications for Earth's and lunar cores, *Earth Planet. Sci. Lett.*, 262, 182–186, doi:10.1016/j.epsl.2012.11.042.
- Nittler, L. R., et al. (2011), The major-element composition of Mercury's surface from MESSENGER X-ray spectrometry, *Science*, 333(6051), 1847–1850, doi:10.1126/science.1211567.
- Padovan, S., J. L. Margot, S. A. Hauck, W. B. Moore, and S. C. Solomon (2014), The tides of Mercury and possible implications for its interior structure, *J. Geophys. Res. Planets*, 119, 850–866, doi:10.1002/2013JE004459.

- Peale, S. J. (1973), Rotation of solid bodies in the solar system, *Rev. Geophys.*, *11*(4), 767–793, doi:10.1029/RG011i004p00767.
- Peale, S. J. (1976), Does Mercury have a molten core?, *Nature*, *262*, 765–766, doi:10.1038/262765a0.
- Peale, S. J. (1988), The rotational dynamics of Mercury and the state of its core, in *Mercury*, edited by F. Vilas, C. R. Chapman, and M. S. Matthews, pp. 461–493, Univ. of Arizona Press, Tucson, Ariz.
- Peale, S. J., R. J. Phillips, S. C. Solomon, D. E. Smith, and M. T. Zuber (2002), A procedure for determining the nature of Mercury's core, *Meteorit. Planet. Sci.*, *37*(9), 1269–1283, doi:10.1111/j.1945-5100.2002.tb00895.x.
- Pettengill, G. H., and R. B. Dyce (1965), A radar determination of the rotation of the planet Mercury, *Nature*, *206*, 1240, doi:10.1038/2061240a0.
- Plagemann, S. (1965), A model of the internal constitution and temperature of the planet Mercury, *J. Geophys. Res.*, *70*(4), 985–993, doi:10.1029/JZ070i004p00985.
- Poirier, J.-P. (2000), *Introduction to the Physics of the Earth's Interior*, 2nd ed., 312 pp., Cambridge Univ. Press, Cambridge, U. K.
- Riner, M. A., C. R. Bina, M. S. Robinson, and S. J. Desch (2008), Internal structure of Mercury: Implications of a molten core, *J. Geophys. Res.*, *113*, E08013, doi:10.1029/2007JE002993.
- Rivoldini, A., and T. Van Hoolst (2013), The interior structure of Mercury constrained by the low-degree gravity field and the rotation of Mercury, *Earth Planet. Sci. Lett.*, *377–378*, 62–72, doi:10.1016/j.epsl.2013.07.021.
- Rivoldini, A., T. Van Hoolst, and O. Verhoeven (2009), The interior structure of Mercury and its core sulfur content, *Icarus*, *201*(1), 12–30, doi:10.1016/j.icarus.2008.12.020.
- Rivoldini, A., T. Van Hoolst, O. Verhoeven, A. Mocquet, and V. Dehant (2011), Geodesy constraints on the interior structure and composition of Mars, *Icarus*, *213*, 451–472, doi:10.1016/j.icarus.2011.03.024.
- Rivoldini, A., T. Van Hoolst, and L. Noack (2014), Insights into Mercury's interior structure from geodesy measurements and global contraction EPSC Abstracts, *9*, EPSC2014-556.
- Sanloup, C., and Y. Fei (2004), Closure of the Fe–S–Si liquid miscibility gap at high pressure, *Phys. Earth Planet. Inter.*, *147*(1), 57–65, doi:10.1016/j.pepi.2004.06.008.
- Sanloup, C., F. Guyot, P. Gillet, G. Fiquet, M. Mezouar, and I. Martinez (2000), Density measurements of liquid Fe–S alloys at high-pressure, *Geophys. Res. Lett.*, *27*(6), 811–814, doi:10.1029/1999GL008431.
- Sanloup, C., G. Fiquet, E. Gregoryanz, G. Morard, and M. Mezouar (2004), Effect of Si on liquid Fe compressibility: Implications for sound velocity in core materials, *Geophys. Res. Lett.*, *31*, L07604, doi:10.1029/2004GL019526.
- Schubert, G., P. Cassen, and R. E. Young (1979), Subsolidus convective cooling histories of terrestrial planets, *Icarus*, *38*(2), 192–211, doi:10.1016/0019-1035(79)90178-7.
- Schubert, G., M. Ross, D. Stevenson, and T. Spohn (1988), Mercury's thermal history and the generation of its magnetic field, in *Mercury*, edited by F. Vilas, C. R. Chapman, and M. S. Matthews, pp. 429–460, Univ. of Arizona Press, Tucson, Ariz.
- Seagle, C. T., A. J. Campbell, D. L. Heinz, G. Shen, and V. B. Prakapenka (2006), Thermal equation of state of Fe₃S and implications for sulfur in Earth's core, *J. Geophys. Res.*, *111*, B06209, doi:10.1029/2005JB004091.
- Selivanov, E. N., A. D. Vershinin, and R. I. Gulyaeva (2003), Thermal expansion in troilite and pyrrhotine in helium and air, *Inorg. Mater.*, *39*(10), 1097–1102, doi:10.1023/A:1026007729489.
- Shen, G., H.-K. Mao, R. J. Hemley, T. S. Duffy, and M. L. Rivers (1998), Melting and crystal structure of iron at high pressures and temperatures, *Geophys. Res. Lett.*, *25*(3), 373–376, doi:10.1029/97GL03776.
- Siebert, J., V. Malavergne, F. Guyot, R. Combes, and I. Martinez (2004), The behaviour of sulphur in metal-silicate core segregation experiments under reducing conditions, *Phys. Earth Planet. Inter.*, *143–144*, 433–443, doi:10.1016/j.pepi.2003.07.022.
- Smith, D. E., M. T. Zuber, R. J. Phillips, S. C. Solomon, S. A. Hauck, F. G. Lemoine, E. Mazarico, G. A. Neumann, S. J. Peale, and J. L. Margot (2012), Gravity field and internal structure of Mercury from MESSENGER, *Science*, *336*(6078), 214–217, doi:10.1126/science.1218809.
- Solomon, S. C. (1977), The relationship between crustal tectonics and internal evolution in the moon and Mercury, *Phys. Earth Planet. Inter.*, *15*(2), 135–145, doi:10.1016/0031-9201(77)90026-7.
- Spohn, T. (1991), Mantle differentiation and thermal evolution of Mars, Mercury and Venus, *Icarus*, *90*(2), 222–236, doi:10.1016/0019-1035(91)90103-Z.
- Stevenson, D. J. (1983), Planetary magnetic fields, *Rep. Prog. Phys.*, *46*(5), 555, doi:10.1088/0034-4885/46/5/001.
- Stevenson, D. J., T. Spohn, and G. Schubert (1983), Magnetism and thermal evolution of the terrestrial planets, *Icarus*, *54*(3), 466–489, doi:10.1016/0019-1035(83)90241-5.
- Stewart, A. J., M. W. Schmidt, W. van Westrenen, and C. Liebske (2007), Mars: A new core-crystallization regime, *Science*, *316*(5829), 1323–1325, doi:10.1126/science.1140549.
- Strom, R. G., N. J. Trask, and J. E. Guest (1975), Tectonism and volcanism on Mercury, *J. Geophys. Res.*, *80*(17), 2478–2507, doi:10.1029/JB080i017p02478.
- Tosi, N., M. Grott, A.-C. Plesa, and D. Breuer (2013), Thermochemical evolution of Mercury's interior, *J. Geophys. Res. Planets*, *118*, 2474–2487, doi:10.1002/jgre.20168.
- Urakawa, S., K. Someya, H. Terasaki, T. Katsura, S. Yokoshi, K. I. Funakoshi, W. Utsumi, Y. Katayama, Y. I. Sueda, and T. Irifune (2004), Phase relationships and equations of state for FeS at high pressures and temperatures and implications for the internal structure of Mars, *Phys. Earth Planet. Inter.*, *143–144*, 469–479, doi:10.1016/j.pepi.2003.12.015.
- Van Hoolst, T., and C. Jacobs (2003), Mercury's tides and interior structure, *J. Geophys. Res.*, *108*(E11), 5121, doi:10.1029/2003JE002126.
- Van Hoolst, T., F. Sohl, I. Holin, O. Verhoeven, V. Dehant, and T. Spohn (2007), Mercury's interior structure, rotation, and tides, *Space Sci. Rev.*, *132*(2–4), 203–227, doi:10.1007/s11214-007-9202-6.
- Van Hoolst, T., A. Rivoldini, R.-M. Baland, and M. Yseboodt (2012), The effect of tides and an inner core on the forced longitudinal libration of Mercury, *Earth Planet. Sci. Lett.*, *333–334*, 83–90, doi:10.1016/j.epsl.2012.04.014.
- Vander Kaaden, K. E., and F. M. McCubbin (2015), Exotic crust formation on Mercury: Consequences of a shallow, FeO-poor mantle, *J. Geophys. Res. Planets*, *120*, 195–209, doi:10.1002/2014JE004733.
- Verhoeven, O., P. Tarits, P. Vacher, A. Rivoldini, and T. Van Hoolst (2009), Composition and formation of Mercury: Constraints from future electrical conductivity measurements, *Planet. Sci. Lett.*, *57*(3), 296–305, doi:10.1016/j.pss.2008.11.015.
- Watters, T. R., M. S. Robinson, and A. C. Cook (1998), Topography of lobate scarps on Mercury: New constraints on the planet's contraction, *Geology*, *26*(11), 991–994, doi:10.1130/0091-7613(1998)026<0991:TOLSOM>2.3.CO;2.
- Watters, T. R., S. C. Solomon, M. S. Robinson, J. W. Head, S. L. André, S. A. Hauck II, and S. L. Murchie (2009), The tectonics of Mercury: The view after MESSENGER's first flyby, *Earth Planet. Sci. Lett.*, *285*(3), 283–296, doi:10.1016/j.epsl.2009.01.025.
- Weider, S. Z., L. R. Nittler, R. D. Starr, T. J. McCoy, K. R. Stockstill-Cahill, P. K. Byrne, B. W. Denevi, J. W. Head, and S. C. Solomon (2012), Chemical heterogeneity on Mercury's surface revealed by the MESSENGER X-ray spectrometer, *J. Geophys. Res.*, *117*, E00L05, doi:10.1029/2012JE004153.

- Weider, S. Z., L. R. Nittler, R. D. Starr, T. J. McCoy, and S. C. Solomon (2014), Variations in the abundance of iron on Mercury's surface from MESSENGER X-ray spectrometer observations, *Icarus*, 235, 170–186, doi:10.1016/j.icarus.2014.03.002.
- Yseboodt, M., A. Rivoldini, T. Van Hoolst, and M. Dumberry (2013), Influence of an inner core on the long-period forced librations of Mercury, *Icarus*, 226(1), 41–51, doi:10.1016/j.icarus.2013.05.011.
- Yu, X., and R. A. Secco (2008), Equation of state of liquid Fe-17 wt % Si to 12 GPa, *High Pressure Res.*, 28(1), 19–28, doi:10.1080/08957950701882138.
- Zolotov, M. Y., A. L. Sprague, S. A. Hauck II, L. R. Nittler, S. C. Solomon, and S. Z. Weider (2013), The redox state, FeO content, and origin of sulfur-rich magmas on Mercury, *J. Geophys. Res. Planets*, 118, 138–146, doi:10.1029/2012JE004274.